

Transmission, emission and excitation gamma tomography

MASTER'S THESIS

Tímea Hülber

Supervisor: Dr. Dávid Légrády



Budapest University of Technology and Economics

Institute of Nuclear Techniques

2012

Contents

Abstract	iii
Kivonat	iv
1 Motivation	1
1.1 Neutron activation analysis	1
1.2 Compton camera concept	4
1.2.1 Collimation	4
1.2.2 Historical overview	5
1.2.3 Recent applications	6
1.2.4 Main characteristics	7
2 Gamma detection	8
2.1 Position sensitive detection	8
2.1.1 Overview of the options	8
2.1.2 Scintillation crystal combined with position-sensitive PMT	9
2.1.3 MiniPET module	9
2.1.4 Software for detector handling	11
2.1.5 Main characteristics	13
2.2 Coincidence	13
2.2.1 Verification	14
2.2.2 Timing window optimization	14
2.3 Proof of principle	16
2.3.1 Geometry optimization	17
2.3.2 Voltage setting and energy calibration	22
2.3.3 Disregarded effects	22
2.3.4 LYSO own activity	23
2.3.5 Total absorbed energy restriction	24
2.3.6 Illustration of Compton camera concept	25
2.3.7 Conclusion	27
3 Simulation and reconstruction	29
3.1 Monte Carlo simulation	29
3.1.1 Simulation algorithm	29
3.1.2 Comparison with MCNP simulation	31
3.1.3 Optimization	34
3.2 Data storage	36
3.3 Image reconstruction	38

3.3.1	ML - EM method	39
3.3.2	System response matrix	40
4	Experimental setups	41
4.1	Virtual and real $Cs - 137$ source	41
4.1.1	Test of the reconstruction engine	41
4.1.2	Testing imaging capabilities	41
4.1.3	Measured data image reconstruction	43
4.2	Neutron sources	44
4.2.1	Options	45
4.2.2	Comparison	45
4.2.3	Sample selection	46
4.3	NTI Training Reactor	47
4.3.1	Dosimetry calculations	48
4.3.2	Simulation for detector signal	50
4.3.3	Results	51
4.4	KFKI Research Reactor	53
4.4.1	Cold Neutron source	53
4.4.2	Measurement set-up	54
4.4.3	Preliminary results	55
4.4.4	Image reconstruction	57
4.4.5	Suggestions for a repeated experiment	58
4.5	Limitations of the research	58
4.5.1	Detectors	58
4.5.2	Simulation	59
4.5.3	Image reconstruction	59
4.5.4	Neutron source	59
5	Conclusion	60
	Acknowledgment	61
	References	62
	Appendix	66
	List of abbreviations	66
	Önállósági nyilatkozat (Declaration of independent work)	67

Abstract

In this thesis, the idea of combining prompt-gamma neutron activation analysis and gamma detection with Compton-camera concept was investigated. As a consequence of the relaxation of the excited nucleus that had captured a neutron γ -photons are emitted immediately. These prompt particles are characteristic to the target nucleus, hence can be used for analytical analysis. Their detection by a detector configuration with electric collimation increases the detection efficiency. The electric collimation based on two position- and energy-sensitive detectors as a detector system. A photon is Compton scattered in the first detector and afterwards absorbs in the second one. From the released energies and the interaction positions the emitting place of the photon can be determined with an uncertainty of a conical surface.

We used two miniPET detectors produced by the Institute of Nuclear Research, Debrecen. It contains a matrix of LYSO (lutetium-yttrium-orthosilicate) crystal pins coupled to a position-sensitive photomultiplier tube (PSPMT). A dedicated data acquisition software was written and combined with stepping motor moving. This made the whole system to be capable of executing gamma tomography. With a cesium-137 gamma source a proof for the proper working of the Compton camera concept was found.

In order to simulate the behavior of the detector signals we wrote a Monte Carlo simulation software in C. The code was validated with MCNP5, a three-dimensional Monte Carlo particle transport simulation software. The majority of the simulation results were equal within 10%. It was shown that more significant differences are originated from the cross section library differences.

The applicability of four possible neutron sources were investigated. The neutron flux of the plutonium-beryllium (PuBe) neutron source was not enough for producing detectable amount of prompt-gamma photons. The deuterium-tritium (DT) neutron generator can not be used due to authorization limitations. The training reactor of the Institute of Nuclear Techniques (NTI) had too high gamma-background. Finally the solution was the cooperation with the Budapest Neutron Center (BNC) where we could make experiments with ultracold neutrons (energy < 0.5 meV).

An image reconstruction software was made and used on simulated and real measurement data with success. The features of reconstructed images were discussed. The vertical and horizontal resolution significantly differs. In order to improve the vertical performance the number or the size of absorbing detector should be increased.

Kivonat

Munkám során azt a kérdést vizsgáltam, hogy kombinálható-e a prompt-gamma neutron aktivációs analízis módszere Compton-kamerával végzett gamma detektálással. A neutron befogás következtében gerjesztett állapotba kerülő atommag a relaxációja során rövid időn belül gamma fotonokat emittál. Ezek a gamma részecskék jellemzőek az eredeti atommagra, így felhasználhatóak analitikai célokra. A detektálásukat elektronikus kollimálással végezve a detektálási hatások nagymértékben növelhető. Az elektronikus kollimálás egy detektor és a kollimátor együttese helyett két detektor használatán alapul. Ha a foton Compton-szóródik az első detektorban és elnyelődik a másodikban, akkor a két detektorban leadott energia és a kölcsönhatások pontos helyének ismeretében a szóródási szög, és ezzel együtt az a kúppalást is meghatározható, amely tartalmazza a részecske keletkezési helyét.

Az elvégzett kísérletekhez a debreceni Atommagkutató Intézet által gyártott kisátlat PET (pozitron emissziós tomográfia) készülék két detektor modulját használtuk. A detektor LYSO (lutécium-ittrium-ortoszilikát) kristálytűk alkotta mátrixból és egy hozzáillesztett pozícióérzékeny fotoelektronsokszorozóból áll. Külön ehhez a detektor modulhoz készült egy adatgyűjtő és feldolgozó program, amelynek segítségével a tomográfias kísérletek elvégzéséhez szükséges motormozgatás is elvégezhető. Cézium-137 gamma sugárforrás használatával bebizonyítottuk, hogy a ezzel a két detektorral a Compton-kamera elvire épülő gamma detektálás elvégezhető.

A Compton-kamera detektorelrendezés tulajdonságainak vizsgálatához egy Monte Carlo (MC) szimulációs program készült C programozási nyelven. A kód megfelelő működésének validálása MCNP5 MC részecske transzport szimulációval történt. A két program által adott szimulációs eredmények közti különbség többnyire nem haladta meg a 10%-ot. Bebizonyítottuk, hogy az ennél nagyobb hibák a használt hatáskeresztmetszet táblázatok különbségéből adódnak.

Négy különböző neutron forrás alkalmazhatóságát vizsgáltuk. A plutónium-berillium (PuBe) neutron forrásunk neutron fluxusa nem volt elegendő ahhoz, hogy detektálható mennyiségű prompt-gamma fotont keltsen. A deutérium-trícium (DT) neutron generátor használatának az engedélyeztetéséhez szükséges idő hosszúsága vetett gátat. Az Nukleáris Technika Intézet (NTI) oktatóreaktorában való sikeres mérést a túlságosan nagy gamma háttér hiúsította meg. Végül lehetőséget kaptunk méréseink elvégzésére a csillebéri Budapesti Neutron Központban, ahol a neutronnyaláb energiája nem haladja meg a 0.5 meV-ot.

Iteratív képrekonstrukciós szoftverünket sikeresen használtuk szimulált és mérési eredményeinken. A fenti módszerrel leírt képalkotás legjellemzőbb tulajdonsága, hogy a vízszintes és függőleges térbeli felbontás lényegesen eltér egymástól. Így a további vizsgálatokra nézve javasoljuk az abszorbens detektor mozgatását vagy méretbeli megnövelését, esetleg több detektor együttes használatát.

1 Motivation

In medical imaging there are several successfully evolved and used techniques for determining the spatial distribution of certain quantities. For example: CT (Computed Tomography) measures the spatial distribution of the attenuation coefficient of the medium; PET (Positron Emission Tomography), SPECT (Single Photon Emission Tomography) and gamma camera provide information about the location of specific radioactive nuclei; Two common disadvantages can be mentioned of the methods listed above:

- To inquire spatial distribution, collimator should be used. Traditionally they are mechanical collimators and their efficiency decreasing with increasing energy.
- They either can not acquire information about non-radioactive elements without using any tracing component. Or they are not able to trace the elements separately and simultaneously, just deduce their presence from a typical value range of the measured continuous quantity (e.g.: attenuation coefficient).

These two points can be solved with our concept of combining prompt- γ tomography and gamma detection based on Compton camera. The two basic physical phenomena that is used are the following:

1. **Activation step:** Following a neutron capture the target nucleus emits characteristic γ -photons.
2. **Detection with Compton-camera:** The created γ particles are detected with a special detector system that use a so-called electric collimation instead of mechanical.

The characteristic feature of the γ -energies makes the method capable of precisely determining the elements contained in the sample simultaneously. And the Compton camera concept assures the high efficiency of the detection system even at higher energy ranges. These two phenomena are detailed in the next subsections.

Our main purpose was to try this theory in practice. Since we did not have ideal equipments the goal was to gather information and suggest aspects that should be taken into consideration in a further research working on optimization.

1.1 Neutron activation analysis

In our scope of interest there are two main neutron-matter interaction types that can produce emitted γ -photons characteristic to the target material, thus it can use for analytical purposes. The inelastic scattering is a $(n,n')\gamma$ reaction. It can be triggered by neutrons with high energy. There are already a few preliminary work that has studied the

medical application of the combination of inelastic neutron scattering and tomography. This method is so-called neutron stimulated emission computed tomography (NSECT). It was used for diagnosis of liver iron overload disorders and breast cancer staging ([KST⁺09] and [JSB⁺07]).

The other option is the radiative neutron capture: (n,γ) . It is the dominant interaction type on lower energy ranges. The latter one is detailed below.

There are three types of neutron activation analysis (NAA). If the irradiation and the detection of the emitted γ -photons are separated in space and time, the method called "traditional" neutron activation analysis. In the case of prompt- γ neutron activation analysis (PGAA) the activation and the measurement happens in the same time. The third type is the neutron resonance capture analysis (NRCA), which based on the capture of the neutrons in the way of resonance. Hereinafter the PGAA is described. Respect to medical physics applications the great advantage of PGAA over the conventional activation analysis is that lower neutron flux is needed in order to detect enough γ -photons. This point is important when we want to examine a chemical element distribution in a biological sample, for example in a mouse, since the absorbed dose is a question of matter. Besides its many conventional applications, PGAA has medical use as well such as human body elemental analysis (total body nitrogen, chlorine [DLS⁺98], [S95]). Its combination with tomography set-up is promising as well [GX04] for examining non-radioactive elements (Gd, Cd, Hg and B) that can not be done with SPECT (Single Positron Emission Computed Tomography) or PET (Positron Emission Tomography). The critical aspect whether a good quality image can be done without overdosing the small animal. According to Xu et al. the absorbed dose to a 30-gram mouse by PGI (Neutron flux: $108 \frac{1}{cm^2s}$, 30-min scan time) is equivalent to that when the mouse is scanned by a combined PET/CT (Computed Tomography) system (CT:40 kVp/0.500 mmAl/250 ms/400 μ A, PET: 100 μ Ci 18F). In our case, we used only dead materials as a phantom since the purpose of this work to demonstrate the possibility of the combination of PGAA and electric collimation. However later on the examination can be extended to biological entities.

Let us move on to the details of the prompt-gamma neutron activation process. When a nucleus (A_ZX) captures a neutron, a compound nucleus is formed in an excited state. Its extra energy equals with the binding energy of the neutron (7-9 MeV), since the kinetic energy of the neutron is negligible. The excited nucleus can relax through several different ways producing γ photons and maybe charged particles as well. The principle source of the analytical signal is the radiative neutron capture. During the relaxation of the compound nucleus to a stable nucleus characteristic prompt- γ -photons are emitted within 10^{-12} s. The energy and the intensity of these particles is characteristic to the nucleus with $(A+1)$ atomic number, therefore indirectly to the original nucleus as well. See Figure 1(a) and 1(b). In most cases the stable configuration yields a radioactive

nucleus which mostly decays with β^- decay, but the electron capture and β^+ decay are possible as well. Some cases the so-called decay- γ -photons coming from these relaxation processes can be used for PGAA analysis as well. [SK10].

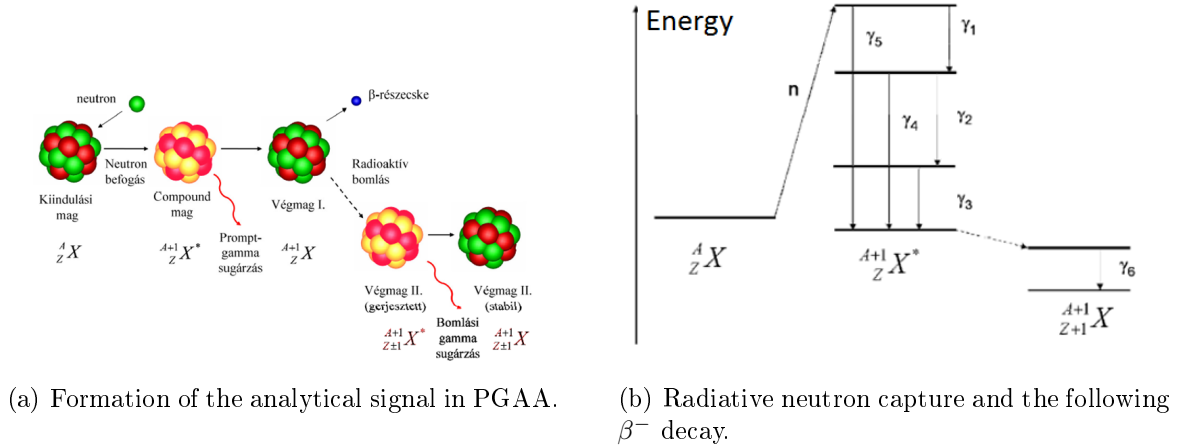


Figure 1: Illustrations for PGAA.

The general benefits of PGAA technique are listed below:

- Excluding 4He all of the other nuclides can go through neutron capture, hence this method theoretically is suitable for detecting the presence of every element simultaneously.
- There is a low proportion of transformed nuclei compared to traditional NAA, thus the rates of isotopes remain the same. This method can be used for analysis of valuable objects or biological samples, because it is non-destructive.
- Most of the cases the remaining activity of the sample is negligible.
- The energy and the intensity of the detected γ -photons depends on the structure of the nuclei, not on the chemical environment.
- Using neutrons with energy large enough, the analysis is volumetric, contrary to other analytical methods. Thus in the case of PGAA the concentration information accumulated in the analytical signal is an average value over the whole sample volume. This feature makes the PGAA feasible for tomography purposes. However neutrons having low energy only a superficial analysis can be done.
- Statistical approximation can be used for assessing the uncertainty of the measurement result. The accuracy of the result can be improved by the extension of the measurement time.

1.2 Compton camera concept

1.2.1 Collimation

In order to provide angular information for gamma-tomography in general, mechanical collimators are used for collimation. These lead sheets work as a direction filter which allows only those photons to pass through that have a certain direction, and absorb all of the others. Demonstrate the main disadvantage of this collimation method two feature is introduced here:

1. The resolution of the collimator can be described with the broadening of the image of a point source :

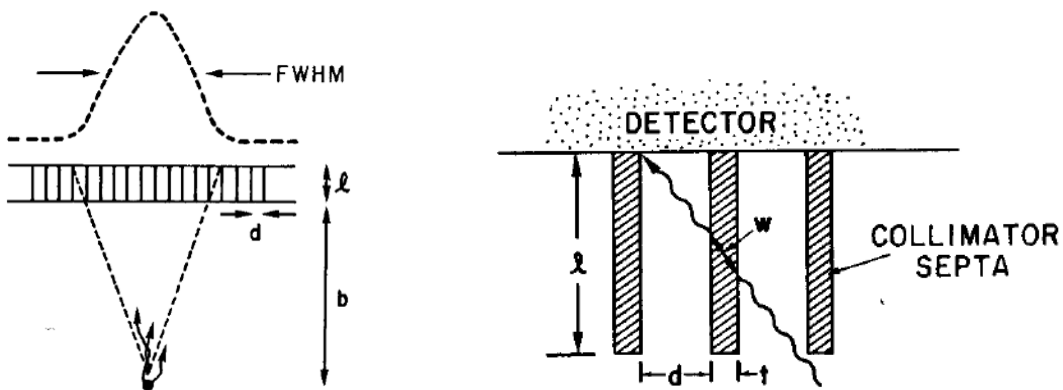
$$R_c = \frac{d(l+b)}{l},$$

where d is the size of the collimator holes, l is the width of the collimator and b is the distance between the point source and the collimator surface (see Figure 2(a)).

2. The efficiency of the collimator, i.e. the proportion of the γ -photons that are detected by the detector laying after the collimator to the total number of emitted photons, is:

$$\eta = \kappa^2 \left(\frac{d}{l}\right)^2 \frac{d^2}{(d+t)^2},$$

where κ is a material parameter and t is the width of the collimator septa (see Figure 2(b)).



(a) Formation of the spatial resolution of the mechanical collimator

(b) Demonstration for the collimator's efficiency

Figure 2: Mechanical collimation

There is an inverse connection between the resolution and the efficiency. With the increment of the d/l ratio the resolution is improving (R_c decreases) and the efficiency

is declining (η decreases). It means that the wider septa allows fewer photons to go through on itself, decreasing the efficiency. But in the same time fewer photons arrive to the detector from a direction which deviates from the requires one, so the resolution becomes better.

Regarding the photon energy, the goodness of the mechanical collimation get worse on high energy ranges. Because photons with high energy do not tend to interact, so they go through the collimator septa without absorption. Since in PGAA analysis most of the characteristic energy levels are above 500 keV another approach eliminating the problem with high energies would be beneficial. For a photon beam having 500 keV energy needs 4 mm of lead to decrease its intensity to the half of the original one. The same half width for 1 MeV photons is 72mm. Thus it would require quite wide collimator septum.

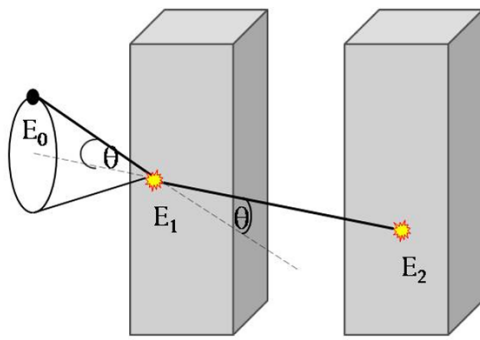
The concept of electric collimation, or with other name Compton-camera, was first proposed by Pinkau and White as well separately from each other in 1966 and 1968. Instead of one gamma detector they placed two position-sensitive detectors after each other. If a photon does a Compton scattering in the first detector and a photoabsorption in the second detector, then knowing the positions of the interactions, the released energy in one of the detectors and the original energy or the second absorbed energy, the angle of the occurred scatter can be calculated. Hence the notion scatterer used for the first detector and absorber for the second one. The path of a selected photon is demonstrated in Figure 3(a). The connection between the original energy (E_0) and the energy after the Compton scattering (E_2) can be written as follows:

$$E_2 = \frac{E_0}{1 + \frac{E_0}{m_0c^2}(1 - \cos(\Theta))}, \quad (1)$$

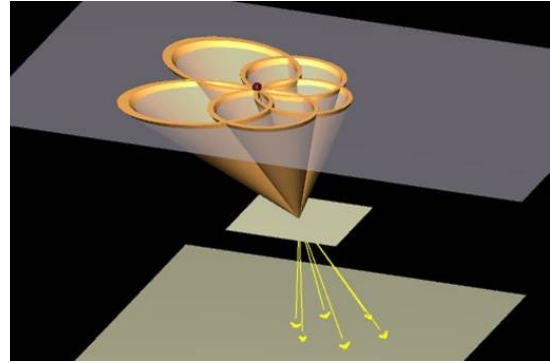
where Θ indicates the angle between the original direction of the photon and its direction after the interaction, $m_0c^2 = 511$ keV is the rest energy of an electron. Therefore, from the calculated scattering angle we can construct a conical surface from where the photon expected to be emitted (see Figure 3(b)). An image from the source object can be reconstructed using the data collected with the two detectors.

1.2.2 Historical overview

A half decade after Pinkau and White firstly proposed the concept of electric collimation, Schönfelder built the first equipment based on it for astrophysics purposes [SHS73]. It contained two huge scintillation blocks. The possibility of the medical application was introduced by Todd and Nightingale in 1974. The first prototype for non-astrophysical goals was constructed by Singh in 1983 [Sin83]. He used high purity germanium (HPGe) detectors as the scatterer detector instead of the formerly used NaI detectors which improved the detection efficiency and energy resolution. Martin and Gormley changed the



(a) The examined type of photon pathway: Compton scattering in the first detector and photoabsorption is the second detector.



(b) From the position of the interactions and the released energies a conical surface can be calculated from where the photon came from.

Figure 3: Compton camera concept

geometry of the detectors [MKW⁺93]. In astrophysics the challenge is dealing with high energy ranges but in medical applications the typical energies are below 600 keV. In this range after Compton scattering the new photons directions are spread out over a wider range of angles according to the Klein-Nishina formula. Thus placing the absorber detector not in front of the first one but beside of it is a great advantage. Expanding this concept in space the form of the absorber should be a ring detector around the first one. The name of their construction was Single Photon RING Tomography (SPRINT). In 1999 LeBlanc exchanged the scintillation detectors for silicon semiconductor detectors [LCH⁺97]. The improvement of this step was that the silicon do not have to be cooled as the germanium and its spatial resolution is better as well. Furthermore, the ratio of Compton scattering cross section to the total cross section is higher than in the case of germanium that has larger atomic number. Nowadays, mainly so-called double sided strip detectors (DSSD) are used that can handle two dimensional position sensation. Therefore the main development direction concentrates on the more and more complex and faster electronics required by them.

1.2.3 Recent applications

The development of Compton telescopes are still ongoing, since at high energies the mechanical collimation has great handicaps. For example the MEGA project is a mission that enables a sensitive all-sky survey of the medium-energy gamma-ray sky (0.4 - 50MeV) [BRM⁺06b]. Another example is the Tracking and Imaging Gamma-Ray Experiment (TIGRE) [BOA⁺04] which is a prototype balloon-borne telescope for observing gamma-rays in the MeV energy range. It uses multi-layers of thin silicon detectors.

More research group is working on Compton camera developments for medical appli-

ation. Its advantage over nuclear medicine equipments such as PET or SPECT, that a really complex geometry can be worked out. Due to the ability of the camera to gather angular information about the examined object without the need to be placed more module around it or moved around it, the size of a set-up can be reduced compared to the large ring-shaped head of PET or SPECT. With other words it has a wide field-of-view. A Japanese group is examining this possibility with a module with multi-head Si/CdTe which is capable of three-dimensional imaging [YKS⁺11].

Another approach to make a compact Compton camera is done by a Korean research group [SKP⁺10]. They are using two DSSDs and a NaI(Tl) detector for constructing a multi-scatter camera. Normally, several layers of silicon detectors use as a scatter detector in order to increase the probability of Compton scattering. But here multi-scattering camera refers to a construction which bases on one Compton scattering per each DSSD. The main purpose of it is to maximize the imaging resolution by accurately determining the trajectory of a photon between the two high-spatial-resolution scatterer detectors. However the imaging efficiency is decreasing in the same time. The absorber detector is used only for total energy gating and coincidence counting and, therefore, a position-sensitive detector is not mandatory.

As a third interesting application I would mention Compton camera as a system for hadron therapy monitoring [FZMP10]. Knowing the total amount and location of deposited dose is crucial in hadron therapy, thus a really precise and fast monitoring is needed. The best PET systems still do not quick enough to stop a hadron therapy in an emergency case when the treatment differs from the therapy plan. The Compton camera configuration can be an alternative solution.

1.2.4 Main characteristics

To sum it up, a list is provided below with the main advantages of the Compton camera that the recent applications want to profit from.

- Possibility of high efficiency even at high energies compared to mechanical collimation. Resulting in significant reductions of imaging time and patients radiation exposure.
- Compactness.
- Wide field-of-view. There is no need of rotation for three-dimensional imaging.
- Multi-tracing. Ability to measure several different kinds of radioisotopes simultaneously.

2 Gamma detection for tomography applications

2.1 Position sensitive detection

2.1.1 Overview of the options

Besides the energy detection the other main point of the Compton camera method is the position detection of photon interactions. Two main detector type can be used for this purpose: semiconductor detectors and scintillation detectors. In the beginning of using Compton cameras scintillation crystals (NaI(Tl) and HPGe) coupled with PMTs were used ([SHS79], [Sin83]).

In 1999 LeBlanc ([LeB99]) introduced the Si pad detectors (SPD) to this field, where pad refers to pixel array detector. Its advantages were obvious: working at room temperature, 1keV FWHM (full width at half maximum), mm in spatial resolution, smaller Doppler broadening. As a scatterer detector another benefit of it can be mentioned. Its ratio of Compton scattering cross section to the total cross section is higher than that of the scintillation crystals. So the efficiency for those photon pathways that have one Compton scattering and one photoabsorption is higher with this construction. The SPD is actually a couple of diodes arranged in a matrix. Due to reverse bias a depletion region is formed around the pn junction. When here a particle with charge ionizes the detector material, electron - hole pairs are produced. With their arrival to the electrodes they trigger the electric signal.

The next step was the use of silicon microstrip detectors, further more double-sided strip detectors (DSSD) ([BRM06a], [SLK⁺08]). They contain orthogonally implanted n and p strips on both sides of the detector, which makes them suitable for 2D position detection. With their application the highest spatial resolution can be achieved while keeping the number of detecting channels relatively small in comparison to, for example, pixel detectors.

Another approach of the scintillator - photo-detector couple is based on the idea of replacing the traditionally used photomultipliers with silicon photomultipliers (SiPM). They basically consist of an array of microscopic, parallel connected avalanche photodiodes (APDs) which operate in Geiger mode. In order to avoid the non-linearity of an APD, the micro-cells are biased above breakdown and a couple of them placed next to each other. So supposing that there is only one photon reaches a cell, their cumulative signal will be proportional to the number of incident photons. In other words, we omit the amplitude of the signal and we use a diode only as one bit of information.

One version of this technology is the digital SiPM evolved by Phillips ([FPD⁺09], [DPF⁺09]). The integration of basic electronic processing within the SiPM sensitive area makes it promising. This is the feature with which dSiPM overcomes the problem of

analog SiPMs by early digitization of Geiger-cell output. Namely, a complete trigger logic and a time to digital converter are integrated into the sensor eliminating the need for external processing electronics with all of its handicaps.

Lack of these equipments we could not use the most suitable detectors for a Compton camera. However a great alternative solution arose: two miniPET modules that have a LYSO (lutetium-yttrium-orthosilicate) scintillation crystal and a position-sensitive PMT. Hereinafter, this detector module is going to be described in more detail.

2.1.2 Scintillation crystal combined with position-sensitive PMT

Conventionally every scintillation crystal was coupled to a photomultiplier tube. In the 70's the improvements in this field based on the addition of more tubes. But a certain point, the size of the photomultipliers and the increasing number of read-out channels became the limitation of advancements. A large breakthrough was the introduction of 'block detectors' in 1986 by Casey and Nutt ([CN86]) where a matrix of scintillation crystal is attached to fewer number of PMTs. Thus the light from each crystal is shared among the PMTs. The position of interactions can be calculated from the center of gravity of the PMT's output signal (Anger principle). In 1986 another solution was suggested as a PET detector. Hamamatsu proposed the first PET detector based on a position-sensitive PMT (R2486) ([Uch86]) coupled to a matrix of BGO crystals [GBB⁺09].

2.1.3 MiniPET module

One of the modules I worked with is in the possession of the Institute of Nuclear Techniques (NTI). The other one is kindly lent by the ATOMKI (Institute of Nuclear Research, Debrecen) for this project. One of them contains a 35x35 matrix and the other one contains 33x33 matrix formulated from 1.14x1.14x12 mm^3 LYSO crystal pins and an attached position sensitive PMT produced by Hamamatsu. See Figure 4.

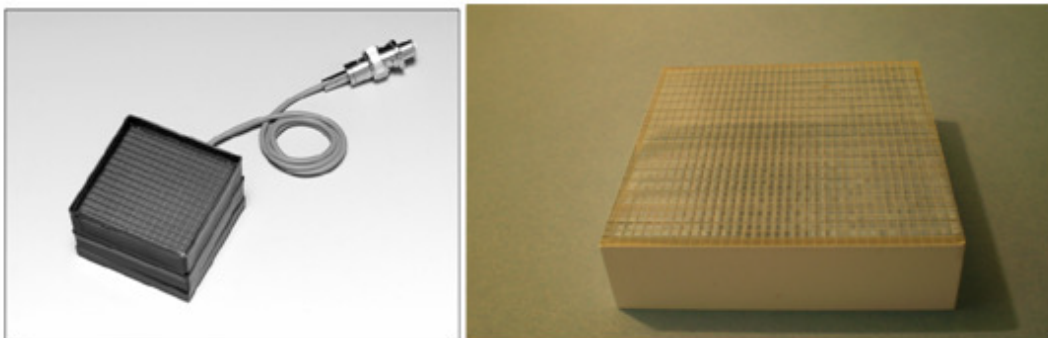


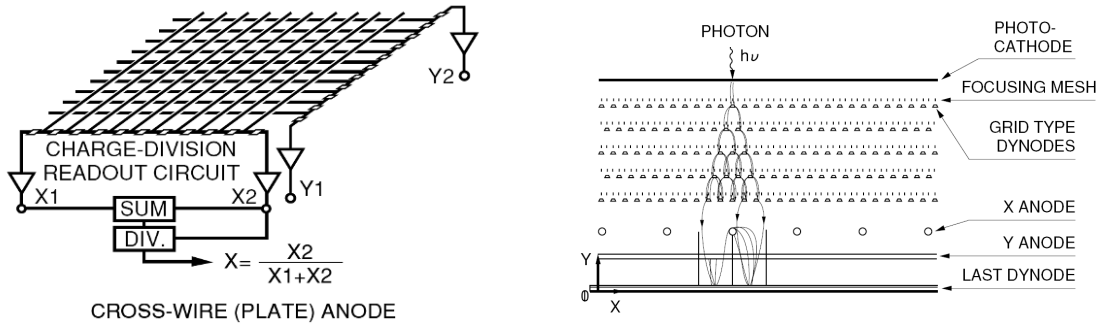
Figure 4: Hamamatsu H9500 multianode PSPMT (left) and matrix of LYSO pin (right) [Laj09]

With the multianode grid and the resistor chain it is possible to determine the position of the interaction and the absorbed energy in the crystal. The scheme of a cross wire PSPMT anode with which the electrons collide is shown in Figure 5(a). The current is divided into two directions (X and Y) according to the ratio of the resistances. Since the wire sections are connected parallel, through the ones with larger resistance less amount of current flows. The collection of the signals happens at the 4 corners of the grid. The notation of them are X_1 , X_2 , Y_1 and Y_2 . These signals are processed independently. Each of them is digitized by an ADC channel and processed with a Xilinx Virtex4 FPGA (Field Programmable Gate Array). The position of the interaction event is derived from the Anger principle:

$$X = \frac{X_1}{X_1 + X_2}, \quad Y = \frac{Y_1}{Y_1 + Y_2}, \quad E = X_1 + X_2 + Y_1 + Y_2 \quad (2)$$

The intensity of the signal is proportional to the received energy, so a scaling will be needed during the data transformation process:

$$x = \frac{X}{E}, \quad y = \frac{Y}{E} \quad (3)$$



(a) Cross wire anode structure of PSPMT in the miniPET module

(b) Electrode structure and electron trajectories

Figure 5: Basics of PSPMT's position detection

The digital number of the energy and x, y position together with a time stamp are transmitted through an Ethernet cable to an acquisition computer for further data analysis. This data acquisition communication is controlled by a Linux OS running on the FPGA. This printed circuit board also include a module for setting the high voltage of the PSPMT. A draft and the real outlook of the detector are shown on Figure 6.

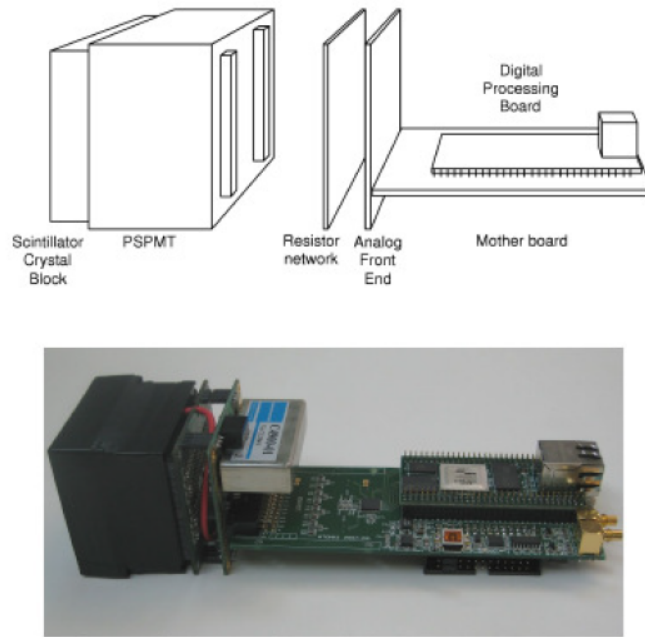


Figure 6: Draft from the parts of the miniPET module and a real photo about it [Laj09]

2.1.4 Software for detector handling

A self-written software was made using C# in order to handle all of the steps from data acquisition to coincidence sorting (Figure 7). It is able to inquire data from the detector which gives the information in a flow of bytes. The mode of data acquisition is in list mode. It means that the data flow contains the parameters of the single events arranged after each other. It transmits all of the data about all of the interactions happened in the detectors. So no coincidence filtering or other analyzing process are made by the detector itself.

There is a definite structure of the data respect to one single event. Lacking any official documentation on it, a short summary is reported here. Among other things, it codes the time stamp, the X, Y amounts and the energy. A summary about it can be read in Table 1.

Of course, these data has discrete values. This is one of the reason that later on a calibration process is required. The transformation of all of these information from binary data flow to ASCII is also conducted by the program. This step includes the rescaling described by Equation 3. At this point a spatial distribution can be plotted separately for each detectors. As the scatterer the detector with the identification number of 42 was used and as the absorber the detector number 15. These identifiers can be seen at the right side of the window signifying which figure corresponds to which detector. Another function of the program does the sorting of coincidence events. The timing window is

	Role	Length (byte)	Position (byte)	Comments
SS	Status bit	2	0-1	For error notification
ER	Event counter	2	2-3	For checking proper data transmission
E	Absorbed energy	4	4-7	Without errors, the first 5 bit = 0
X	X position	4	8-11	Without errors, the first 5 bit = 0
Y	Y position	4	12-15	Without errors, the first 5 bit = 0
TP	Time stamp	8	16-23	Minimal stepsize is 156.25 ps
TE	Time counter	8	14-31	Minimal stepsize is 0.67108864 s
Total		32		

Table 1: Decoding of the data structure of an event

adjustable. There is an option as well to store the data in an ASCII file. Data from all of the events or only from the coincidences can be written into an ASCII file. We need to move the object in order to perform a tomography measurement. This moving was realized with the help of a stepping motor. We used a software written by G. Kleizer to execute the communication between the computer and the motor. The synchronization of data collection and motor moving was done by the same dedicated C# software that was mentioned before in this section.

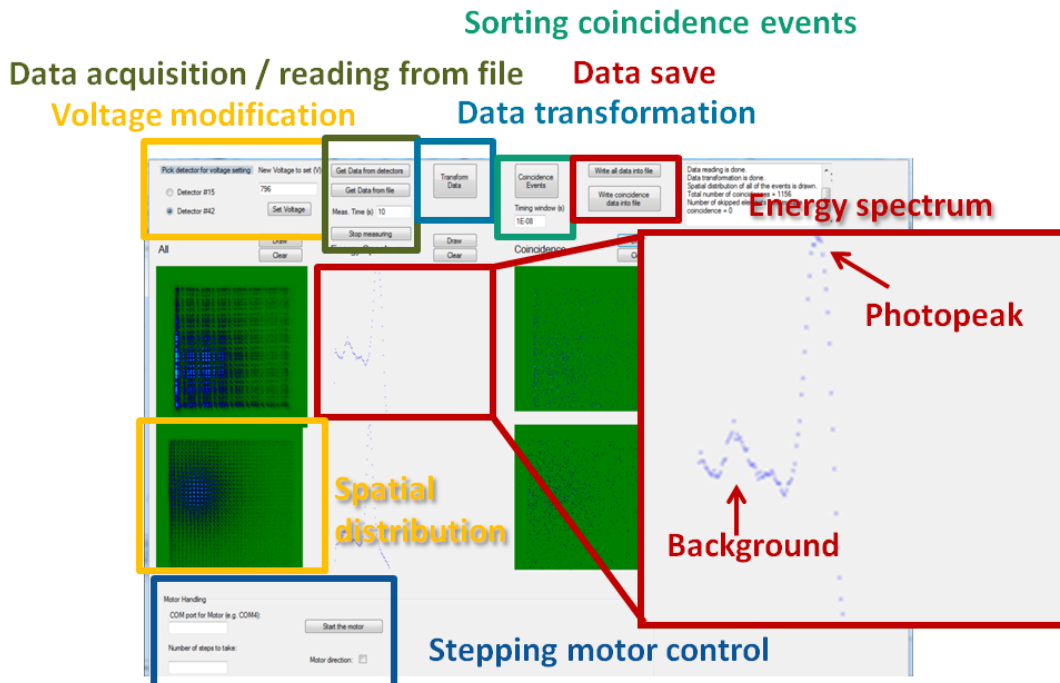


Figure 7: Self-written C# program for data acquisition, transformation, motor movement and coincidence sorting. The energy spectrum and the spatial distribution here represent the data coming from a measurement with $Na - 22$ source.

2.1.5 Main characteristics

The natural lutetium contains 2.95 % ^{176}Lu radioactive isotope which decays to ^{176}Hf with β^- decay. There is no problem with the arisen antineutrino but the escaping electron loses its energy and causes scintillations. Besides, the ^{176}Hf decays produce further γ - photons with 88 keV, 202 keV and 307 keV energy (see Figure 8). The problem is that the decay procedure of the $\text{Hf} - 176$ is a cascade procedure. Thus, the decays do not appear independently in time, but accumulated together in a 4 ps time interval. If one of them is able to escape from the crystal (typically one of the larger ones), we observe a true coincidence with the timing window in the range of ns [Maj11]. At the original application of this miniPET module, this own activity of the crystal does not cause severe problem, because with a high pass filter it can be eliminated, since the energy of interest is 511 keV in the case of positron emission tomography. But unfortunately as it is described in details later on in this dissertaion, the energy range of the lutethium own emission spectrum interfes with the energies examined in the Compton camera set-up.

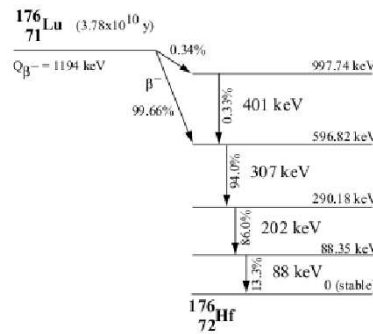


Figure 8: Decay scheme of LYSO spectrum (www.detectors.saint-gobain.com)

2.2 Coincidence

One of the main elements for performing Compton camera imaging is to match the corresponding events occurred in the same time in the two detectors. These event-couples are called coincidence events. The time synchronization between the two detectors are carried out with synchronization cables. In the case of a PET scanner one module gives the timing signal to all of the others. This module gives timing signal to itself as well with a cable that has the same length as the other synchronization cables running to the other modules. Here, we have two detectors tuned together. The resolution of the time stamping in list mode is at the range of 150 ps. A photon can pass through 1 cm in 33 ps, so this does not give limitation comparing with the range of the error of time stamp noting.

2.2.1 Verification

The first basic question before doing coincidence measurements with the two miniPET modules is whether their clocks are really synchronized. The easiest test is to count coincidence events caused by the annihilation photons during $Na - 22$ decay with and without the synchronization cables. Using a source with an activity approximately 340 kBq and 2 cm source - detector distance the number of coincidences in these two cases are 9514 and 7 respectively. The orders of the difference obviously assures that the synchronization is working.

Another probe is to try to make difference between the effect of a source generating coincidence events and another one which has no such a tendency. For example $Na - 22$ and $Cs - 137$. Qualitatively there should be more events that are following each other faster in the case of $Na - 22$ than in the case of $Cs - 137$. Let us calculate the time difference between the adjacent events (they can occur in any of the two detectors) and investigate how many of them are within a small time period (\approx ns), i.e can count as coincidence events. Concerning a series of time intervals rather than only one period of time we can say a verdict without knowing the optimal timing window characteristic to the coincidence events in this set-up. Figure 9 shows the time spectrum of time differences between events following each other in the case of $Na - 22$ and $Cs - 137$ normalized to 1 second and 1 Bq activity. With other words, it represents the number of detected coincidence events per one decay calculated with different time window length. As we expected, for smaller timing windows, which are selective for the coincidence events, the values are higher regarding $Na - 22$. However coincidences do not disappear with the $Cs - 137$ source, there are random coincidences which are still detected. More accurately these events came from either $Cs - 137$ or the LYSO own radiation. Measuring without radioactive source, the contribution from LYSO background could be assessed but only if its activity was known. Anyway, this result also support the proper functioning of the synchronization.

In the case when there is no available radioactive source, an easy check of the proper working of the synchronization cables can be done using the own activity of the lutetium. The two detectors are should be placed parallel next to each other. After filtering for coincidence events the collected data, the spatial distribution of the remaining events should be accumulated along the edge of the detectors facing to each other.

2.2.2 Timing window optimization

After making sure the synchronization works properly the next step toward coincidence detection is to adjust the timing window. The data collection is conducted in list mode. It means that the electronics does not sort out the coincidence events from the

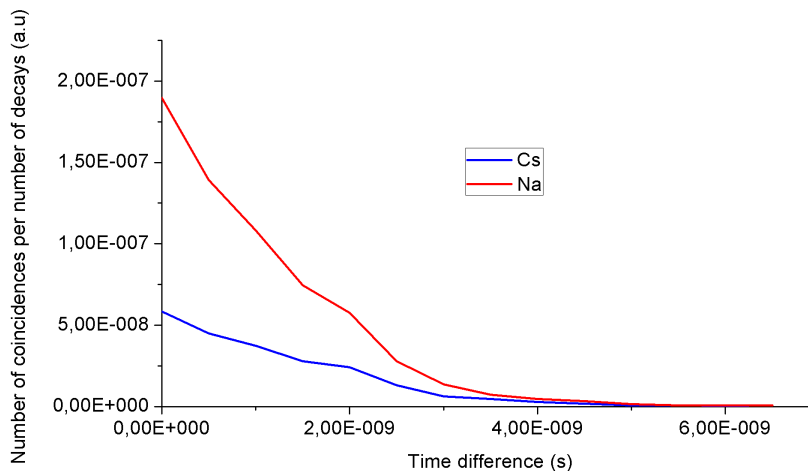


Figure 9: Number of coincidence events per number of decays are higher for smaller timing windows in the case of Na-22 source

data flow but a self-written subroutine as the part of the data acquisition C# program does it. Two events in the two different detector happened close to each other in time are accepted as a coincidence if their time difference is smaller than the timing window. In the case when there are more than two events inside in this time period, all of them are skipped. The reason of this is that it cannot be decided which pair is the right one. If the window is set too wide lots of random coincidences are going to be selected, which results in higher, useless noise level. However choosing the time interval unreasonably short, plenty of true coincidences can be lost. The reason of it is that the time detection also has a Gaussian behavior, so the time difference between coincidence events can be larger than the resolution of the time detection.

The phenomena when two events - each of them is detected in different detector - are signed as coincidence events but they are not caused by the same photon, is called random coincidence. The number of them has an exponential dependence on the frequency of the events registered in the detectors (s_1 and s_2) and the width of the timing window (τ). In first order approximation this connection is linear:

$$cps_{random} \propto 2s_1 \cdot s_2 \cdot \tau$$

The number of multiple coincidence events can be examined as well. Figure 10. demonstrates the dependence of the number of multiple and single coincidence events on the choice of timing window size. In the range of nanoseconds the single coincidences are increasing and there is no multiple coincidences. Around 10 ns there is a saturation of the singles and afterward a decrement. Meanwhile above 100 ns the number of multi-coincidences drastically increasing. This is the region where the time window is so wide

that there is no selection for real coincidence events.

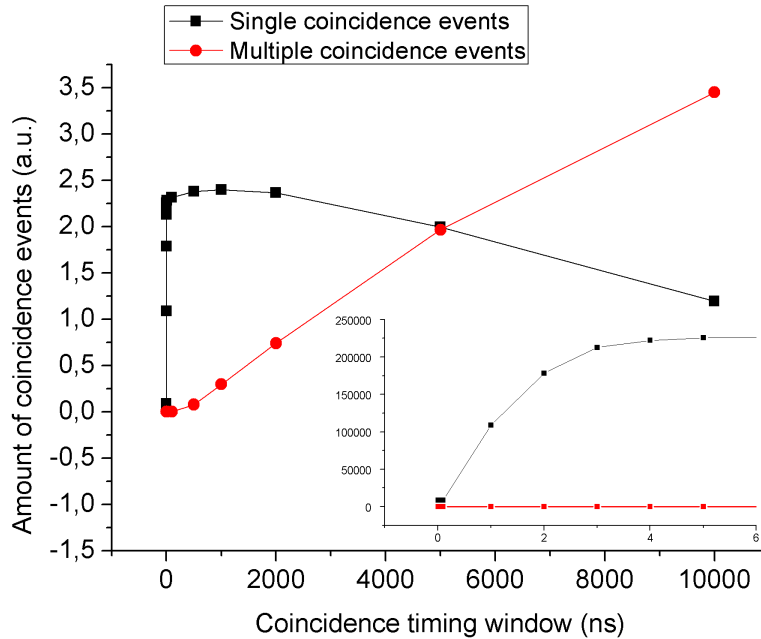


Figure 10: Dependence of the number of multiple and single coincidence events on the choice of timing window. The subfigure shows the magnification of the small time range.

Figure 11 demonstrates the number of coincidence events counted with different timing window settings during a measurement with sodium source. For separating the random coincidences an exponential function was fitted at the end of the curve. It is clear that there is a deviation from exponential shape at smaller time windows. This difference can be explained with the contribution of true coincidences. So according to the graph, the optimal timing window is $2 \cdot 10^{-9}$ s. This corresponds to the point where the measured data starts to differ from the theoretical exponential fit of random coincidences.

For comparison coincidence window optimization was done in [Laj09] as well. Here a mouse and a rat phantom were filled with F^{18} isotope of 7.4 and 25 MBq respectively. The ration of the random and true coincidence events were discussed. The optimal timing window was concluded as 3 ns. The difference can be explained by the variability in the number of the random coincidences regarding different objects and detector set-ups.

2.3 Proof of principle

After the work with coincidence was sorted out another important question was waiting for solution: to demonstrate that the detected event pairs are mainly really coming from single photon interactions (Compton scattering in the first detector and photoabsorption in the second one).

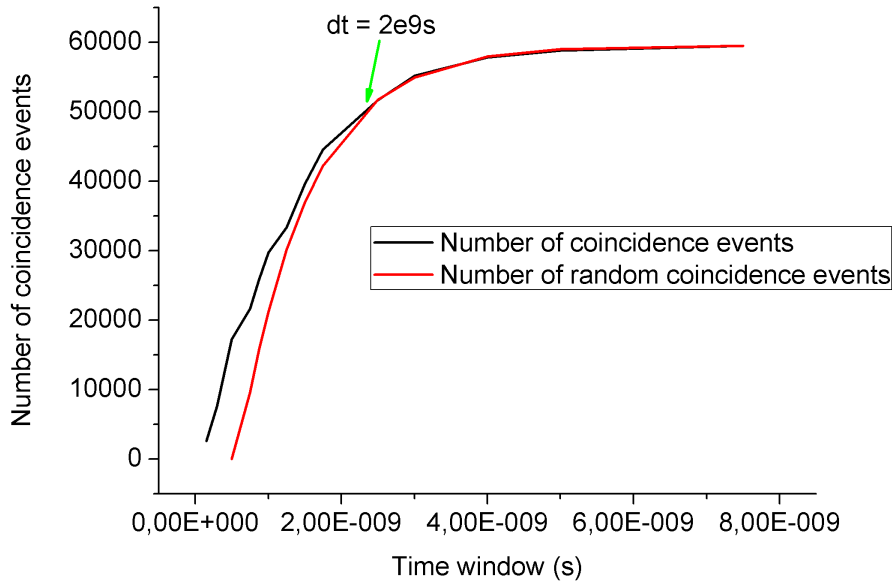


Figure 11: Number of coincidence events versus timing window size

First of all, concentrating only on the phenomenon of the Compton camera a pure gamma source was used. Skipping the neutron activation step just for now, a detector signal without additional noise can be examined. Therefore the gamma ray that needs to be detected became more defined and easily handled. For this purpose a Cs-137 was used. Thus the source energy is $E_0 = 661.7$ keV in the following experiments in this section.

2.3.1 Geometry optimization

Another important point is the detector configuration, i.e. their positions related to each other: distance of the crystal centers, the angle between the direction of a chosen surface.

Traditionally there are two different positioning of the detectors used for Compton camera concept. The easiest when the two detectors are placed after each other with parallel front faces (Figure 12(b)). In this case for efficiency enhancement sometimes a detector with larger surface is used for absorber. This construction has bigger advantage at higher energies since the scattering angle is mainly around 0 for the energies above 500 keV. Though to make difference between the smaller angles better energy resolution is needed. Going towards lower energy ranges, the angular distribution of a scattered beam becomes wider (see Figure 13). Which requires another location for the detectors in order to capture the same number of the scattered photons. For example instead of the plane secondary detector a ring detector is used as the Figure 12(b) demonstrates it.

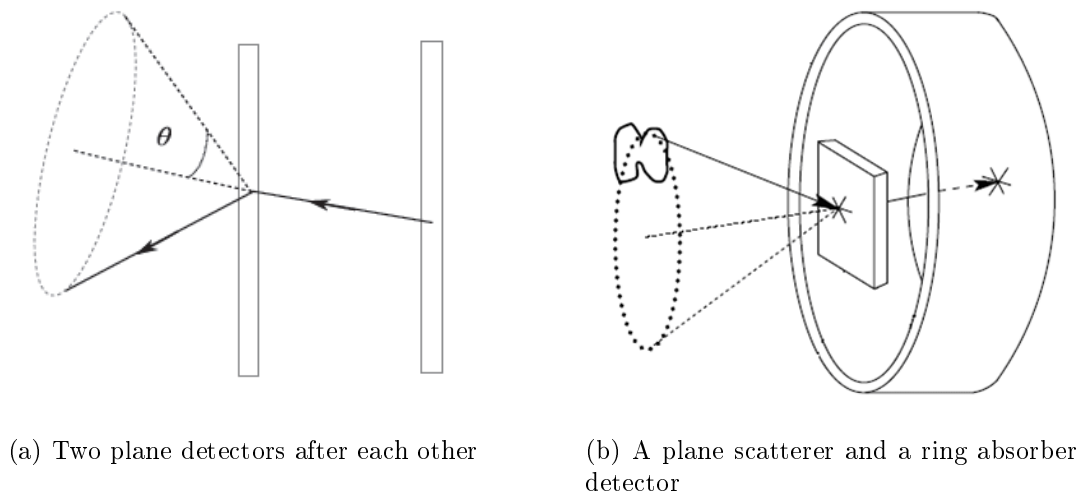


Figure 12: Basic Compton camera arrangements

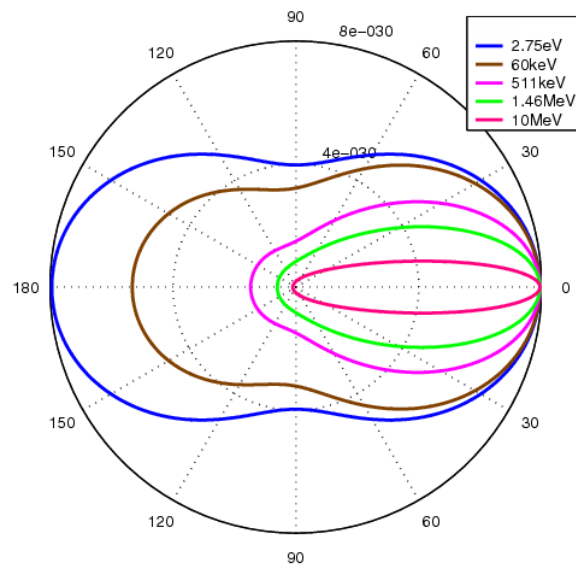


Figure 13: The Klein-Nishina distribution of photon scattering angles over a range of energies.

Adjust these two geometry configuration types to the features of the available detectors we can get the ideas of the Figure 14. Figure 14(b) and 14(c) are only the modification of the ring detector owing to the flatness of the detector. Only a section of the ring is represented by the second detector.

Choosing between the possible configuration is based on several well-defined aspects:

1. Physical properties (e.g. size) of the detectors

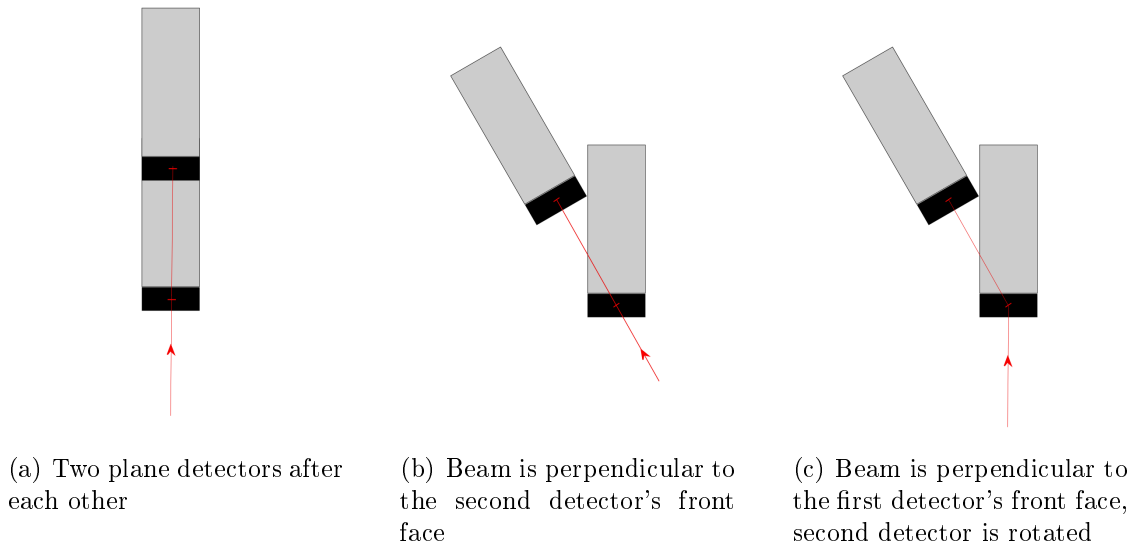


Figure 14: Basic Compton camera arrangements in the case of the miniPET detectors. Red arrow indicates the direction of the pare.

2. Detection efficiency of coincidence events

3. Angular and spatial resolution

4. Angle between the direction of incident photons and the direction of the crystal pins

Physical properties

Considering the miniPET detectors the parallel configuration (Figure 14(a)) is rejected because the physical limitation due to the electronics placed after the scintillation crystals and PSPMTs.

Detection efficiency

In the case of the cesium energy (662 keV) we are dealing with relatively lower energy range, which results in wider scattering angle distribution. That means that the fraction of the photons that endure only a smaller angular deviation (e.g. $< 10^\circ$) from their original direction is lower than the ones changing their direction in a more pronounced way. Therefore their detection in a larger angular distance can lead to higher efficiency.

Angular and spatial resolution

Another point is to examine the minimal angle that can be distinguished from the forward scattering. The main parameter influencing this characteristic is the energy resolution. The FWHM of the photopeak at the spectrum of the $Na - 22$ source with the same voltage settings as used for the experiments described in this section is $85 \text{ keV} \pm 15\%$. The corresponding scattering angle that would result if 85 keV energy is deposited in the first detector can be derived from Equation 1 with rearrangement and using $E_0 = E_1 + E_2$.

Here E_0 indicates the original energy of the particles, E_1 the absorbed energy during Compton scattering and E_2 during the photoabsorption.

$$\cos \theta = 1 - m_0 \cdot c^2 \left(\frac{1}{(E_0 - E_1)} - \frac{1}{E_0} \right) \quad (4)$$

$$E_1 = E_0 - \frac{E_0}{1 + \frac{E_0}{mc^2}(1 - \cos \theta)} \quad (5)$$

According to these formulas the investigated angle range should be at least $27^\circ \pm 4^\circ$.

Incident photon - pin angle

When the particle beam is not parallel with the normal direction of the detector's front, a spatial information lost could occur because the photon interactions in the first detector may correspond to a longer path length in a certain crystal.

According to these considerations the (a) option is excluded because of physical limitations. The energy resolution of the detectors and the corresponding needed angular resolution do not allow the use of the (b) configuration, since with this arrangement maximum 15° angular deviation can be examined. Another disadvantage of the (b) version is that the incident angle of the photons are quite large compared to (a) or (c). So according to the forth aspect the position sensation is not the best in this case. The detection efficiency also supports the (c) variation since the angular distribution of the photons coming from the $Cs - 137$ source according to the Klein-Nishina distribution is quite wide (seen Figure 15).

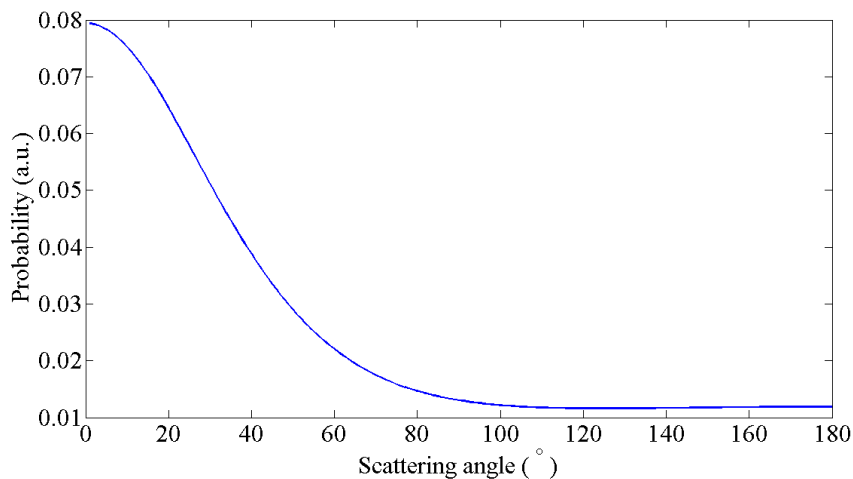


Figure 15: Probability distribution of scattering angle for photons with 661.7 keV energy

To sum it up, the chosen geometry is the third one which fixes how the two detector positions related to each other. Now more details can be optimized. The two remaining free parameters are the inclination between the principal axis of the two detectors (θ) and the distance between their centers.

The position of the second detector (e.g. the center of the crystal) along the first detector is one of the parameters needs to be optimized. The most practical way to choose this is to position the center of the second crystal on the line which go through the middle point of the scatterer crystal and has an angle of θ with the principle axis of the first detector. The benefit of it is that the photons with θ scattering angle hits the central pixels at the absorber.

Choosing the θ angle deeply depends on the application, especially on the energy of the particles of interest. It should be above a minimal angle that was calculated for the energy of the cesium source. Finally the used θ is almost the double of it. The reason of it is to keep open the possibility to compare the results with the latter experiments, where the energy of the particles is 478 keV (see also section 4.2.3). As a result $\theta = 45^\circ$ was set.

A criteria that cannot be accomplished with cesium source is to avoid the energy range of the LYSO's own emission spectrum. That would require a Compton edge higher than ≈ 600 keV or lower than 300 keV, because the LYSO background is significant within this energy interval.

Later on, using detectors configuration and setting with better spatial resolution it is worth to take into consideration the connection between achievable angular distribution depending on the scattering angle: Figure 16. It shows that there is always an angle where the angular resolution is minimal. In our case, this step was omitted since there are larger effects that degrade our resolution.

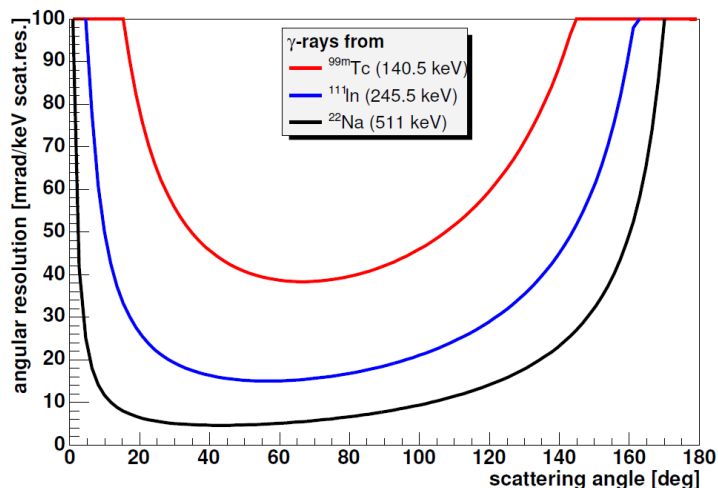


Figure 16: Angular resolution due to finite energy resolution of the scatterer [Stu05]

In the article of Lee et al [LL10] the detector geometry was optimized according to a MCNP5 simulation. For latter improvement their method can be used for optimization as well. The relative standard deviation and FWHM of a reconstructed point source were calculated for a few distances and angles between the detectors, and then the optimized

distance and angle to minimize relative standard deviation without severe degradation of angular resolution were determined.

A notation should be done here regarding non-collimated sources. These angle calculations are only accurate for collimated beams. Generally we have to work with sources expanded spatially and angularly as well. So the scattering angle distribution is more complicated.

2.3.2 Voltage setting and energy calibration

The raw energy data received from the detectors is stored in energy bins. In order to match these bins with real energy intervals a so-called energy calibration has to be carried out. It is heavily depends on the high voltage settings of PSPMTs. The energy calibration was done by using mostly monoenergetic (at least in the used energy range) radionucleids (Table 2).

	Am	Na	Be			
Energy (keV)	59.5	511	81	302	356	384

Table 2: Energy of the calibration sources

In order to adjust the detectable energy with the voltage settings, we have to define the energy range of interest. With the fixed $\theta = 45^\circ$ inclination between the detectors, the 10 cm source - first detector distance and the 4x4 cm² object size few approximative calculations can be done. The maximal possible scattering angle with this geometry is more or less 70°. From Equation 5 the released energy in the first detector can be calculated resulting in this angle: $E_{1,max} = 304.4$ keV. And from this the remaining minimal energy absorbed in the second detector is: $E_{2,min} = 350$ keV. So we have to be able to register the interactions in the detectors that have a released energy between 0 – 350 and 300 – 700 keV respectively in the first and in the second one. Because of the energy resolution, the energy regions are not fitted exactly to the calculated values. Thus a precautionary expansion is applied on the intervals. Gradually tuning the PSPMTs' voltage these criteria were fulfilled. After this adjustments, energy spectra were recorded with the calibration sources. For their photopeaks Gaussian function was fitted. The energy bin where the peak falls is matched with the source's energy. From these channel - energy pairs the energy calibration is made with linear regression.

2.3.3 Disregarded effects

There are a couple of effects that we have now not paid much attention to, but it is worth to take into consideration during the next development stage. The characteristic

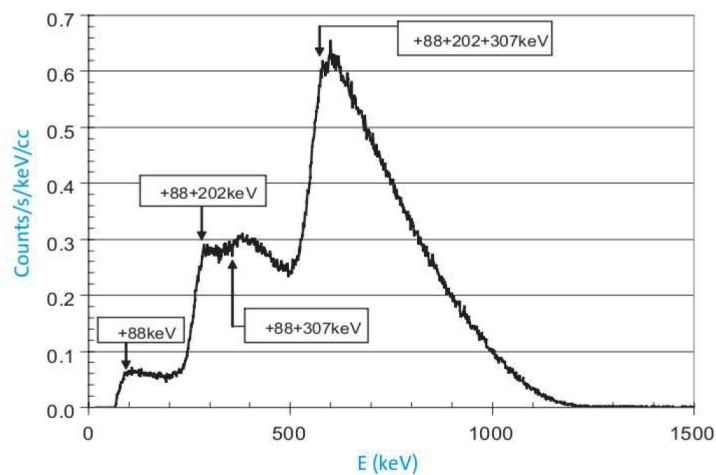
parameters of the PSPMT are not homogeneous. For example quantum efficiency may vary from pixel to pixel, which requires pixel-by-pixel energy calibration. It comes from the phenomenon that the sensitivity of different photocathode areas can differ from each other. This results in spatial dependence of broadening of a photopeak.

2.3.4 LYSO own activity

Unfortunately the background caused by the LYSO crystal is not eliminated together with the effects of neutron activation. Figure 17(b) shows the typical LYSO emission spectrum from the literature. For getting an impression about the ratio of the useful data and the noise Figure 18 was created. Two measurement is compared there. The detector geometry was the same. In the first case, data was collecting without any external source. So the events came from the own emission of the scintillation crystal. In the other case the collimated $Cs - 137$ source described above was used (see Figure 17(a)). The two curve is the energy spectrum of these set-ups in the absorber detector normalized by the time of the measurements. One can conclude based on this figure that the background is extremely high. Later on in this subsection some methods and test are demonstrated whether it is possible to distinguish the signal from the noise and if so, how. Furthermore, we decided to use the source without collimation, increasing the ration of useful activity and LYSO activity. Hereinafter, the results from non-collimated cesium source are described.



(a) Experiment set-up with $Cs - 137$ point source using a lead collimator.



(b) LYSO crystal typical own emission spectrum

Figure 17: Illustration for the experiment with $Cs - 137$ and LYSO crystal.

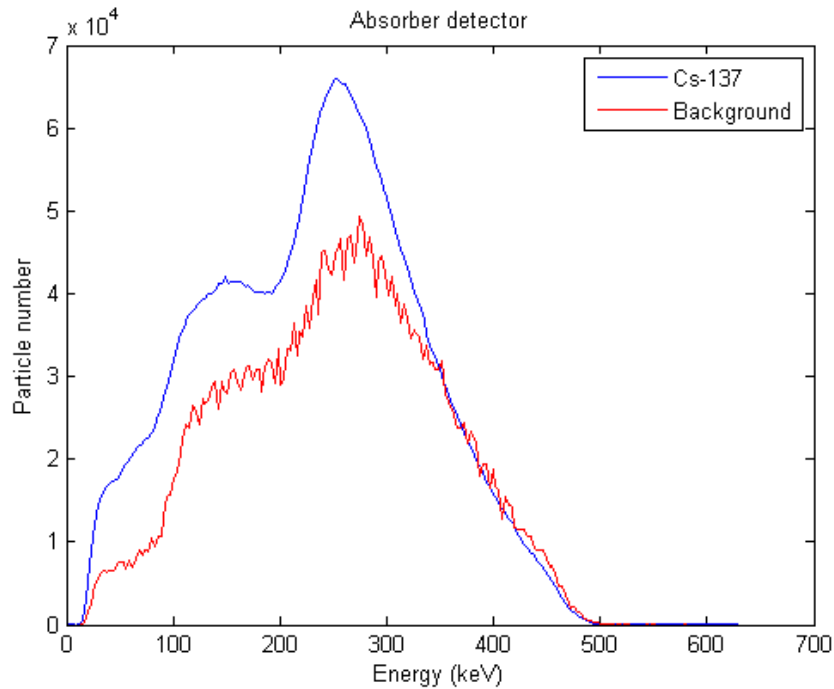


Figure 18: Energy spectrum in the absorber detector with and without $Cs - 137$ source. The background coming from the LYSO crystal own radiation is pretty high.

2.3.5 Total absorbed energy restriction

Coincidence sorting is only one filter that could be used in order to select only those event pairs that belongs to a Compton scattering - total absorption interaction couple. Another useful constriction is to sum the two energies belonging to the two events in the two different detectors. If this total absorbed energy is close to E_0 , it is almost certain that we found a required pair of events. However if the E_0 energy is in the range of the LYSO crystal own emission spectrum, it still has a chance that from mere accident one or both of the events are falsely coming from it. Due to the finite energy resolution of the detector we have to allow a wider energy window for this total energy $E_{tot} = E_1 + E_2$, where E_1 and E_2 now the measured absorbed energies. In the case of cesium the total energy should be between 560 and 760keV.

The validation of using a right total energy window was the following: Several differing timing window was used for coincidence sorting. The proportion of the event pairs whose total energy fall into a 100 keV interval around the energy of the source (661.7 keV) increases with the narrowing timing window. It proclaims that using coincidence sorting those data have larger contribution which really comes from the photons endured one Compton scattering and one photoabsorption. So all of their energy is absorbed in two steps. The error bars are calculated for the assumed Poisson distribution of the particle numbers corresponding to a certain energy interval:

$$\frac{\Delta E_{sum}}{E_{sum}} = \left| \frac{\Delta E_1}{E_1} \right| + \left| \frac{\Delta E_2}{E_2} \right|$$

It is logical that the standard deviation is larger for the event numbers referring to smaller timing periods, since these numbers decrease with the time interval, thus their statistics is worse.

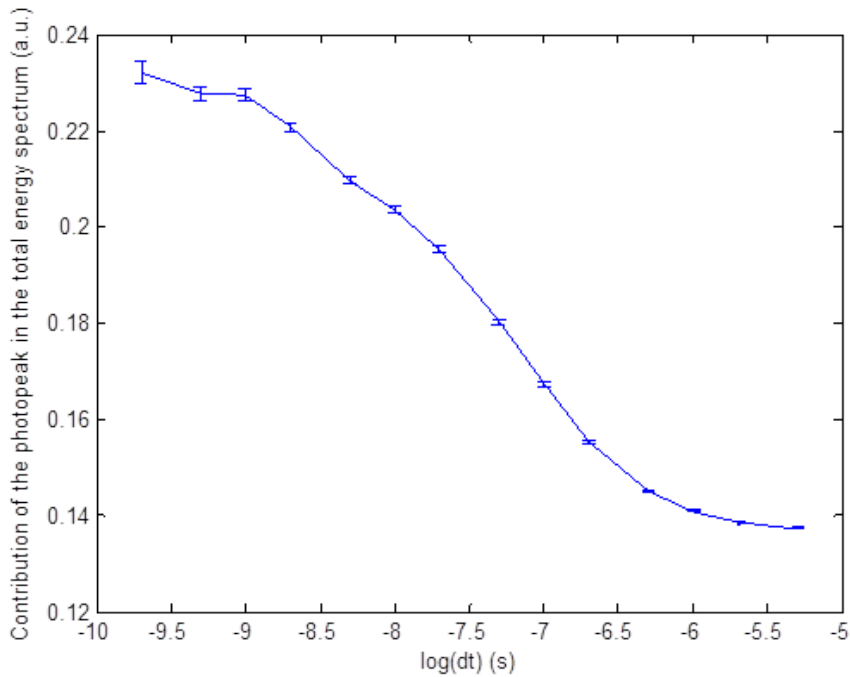


Figure 19: Contribution of the photopeak for more narrow timing windows is larger.

2.3.6 Illustration of Compton camera concept

The main characteristic feature that can be used for the verification of the proof of concept is the relation between the absorbed energy during Compton scattering and the scattering angle. It can be calculated from Equation 4 and 5. The goal of this subsection is to illustrate that the first event from the collected coincidence event pairs has scattered.

Conical sections

The first idea was to select those coincidence events whose first absorbed energy is in a certain energy range which corresponds to a certain scattering angle range according to the formulas above. If the collimation were perfect, so the projection of the source were a point (one pixel) on the first detector, the second events from the selected event-couples would lay on a conic section (ellipse or hyperbola). It could have been a spectacular demonstration but unfortunately more difficulties have emerged. The E_1 energy must be uncertain due to the energy resolution, which results in the broadening of the angular

interval. Finally this causes the blurring of the conic section curve. The other problem is coming from the extent source. Thus the direction of incoming photons are not perpendicular to the detector surface, even not parallel with each other and the first interaction's position is spread out all over the whole detector surface. To sum it up, instead of the examination of the relation between spatial distribution and absorbed energy another approach had to be carried out.

Angular distribution

The next test was the following: A filtering for an energy window around a chosen E_1 energy deposited in the first detector was done as well. Then with coordinate geometry from the location of the source and the position of the linked events the angle of the Compton scattering can be calculated. Due to the E_1 restriction, the angular distribution expected to show a peak as well around the angle corresponds to E_1 . Talking about positions the coordinates of the determined pixel center are meant. Drawing the scattering angle spectrum for the E_1 -restricted data flow, we got the distribution shown on Figure 20. Here the E_1 is between 0 - 100 keV (blue) and 100 - 200 keV (green) which correspond to 0 - 30 and 30 - 48° scattering angle according to Equation 4. There is a significant difference in scattering angle distribution for the two energy interval. However the angle belonging to the maximal value is not equal with the angles expected from the $E_1 - \theta$ relationship. It can be explained with the detector geometry. The angle distribution is the convolution of the angle spectrum based on the Compton scattering and the characteristic function of the detectors' position regarding each other.

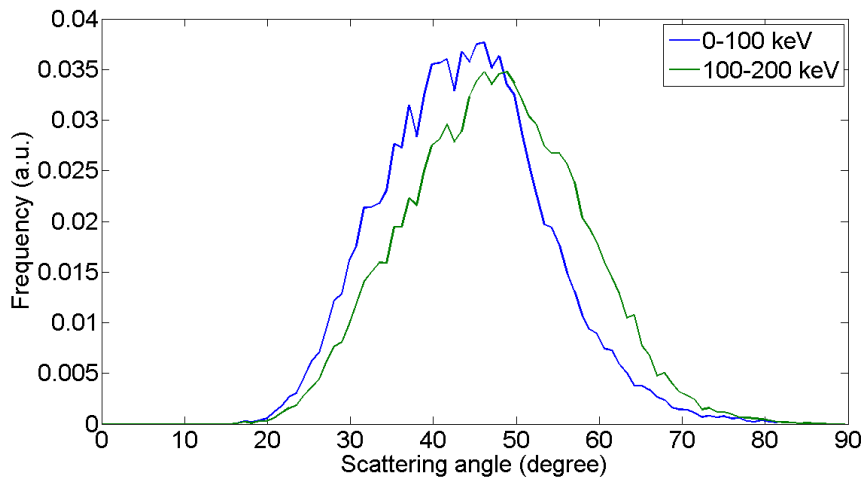


Figure 20: Scattering angle spectrum for restricted coincidence events. The filtering was done according to the absorbed energy in the first detector. Using different energy windows the peak of the scattering angle distribution is shifted.

Scattering angle - first released energy correlation

For more informative visualization a 2 dimensional $\theta - E_1$ correlation test was conducted

(Figure 21). Each pixel signifies the totally absorbed photons (i.e. filtered for the $E_1 + E_2$) whose lost energy in the first detector and scattering angle are inside in given energy and angular interval. On the colormap warmer colors indicate higher number of the events belonged to the chosen pixel. There is a clear correlation between the two examined quantity. The contribution of the LYSO background does not have this kind of definite pattern. Therefore this result assures us that the data can still be used after total energy filtering which eliminates unwanted random coincidences with high efficiency.

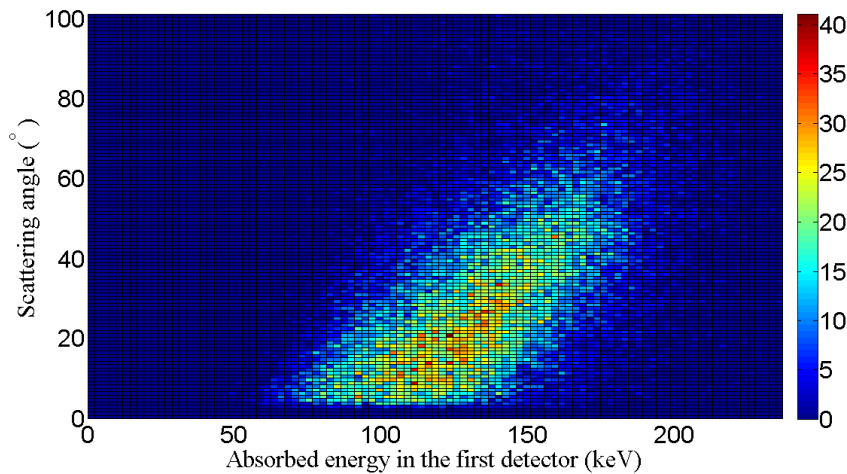


Figure 21: There is a correlation between the absorbed energy in the first detector and the deviation from the original direction of the photons after leaving the first detector.

Figure 22 demonstrates the correlation between the scattering angle and the released energy according to Equation 4. Comparing this calculated curve with the trend coming from the measurement data we can observe that around 45° the two results are equal. This is logical since the detector configuration was tuned for $\theta = 45^\circ$. The difference appears at lower angles. Those detected photons have small scattering angle whose first interaction point is at the left side of the detector (see Figure 23). The left side of the scatterer detector is defined to be the closest side to the absorber detector. This left edge is the one that is the most affected by the LYSO own activity coming from the second detector. Therefore, the deviation of the measurement data is due to the background of the scintillation crystal. Thus we can conclude that at the more significant part of the angular scale the measurement and the expected values are equal.

2.3.7 Conclusion

Finally, based on the tests described above we can state that the phenomenon of the Compton camera concept is working. Therefore, we can go forward to the next stage, to the original idea of producing prompt-gamma photons with neutron activation.

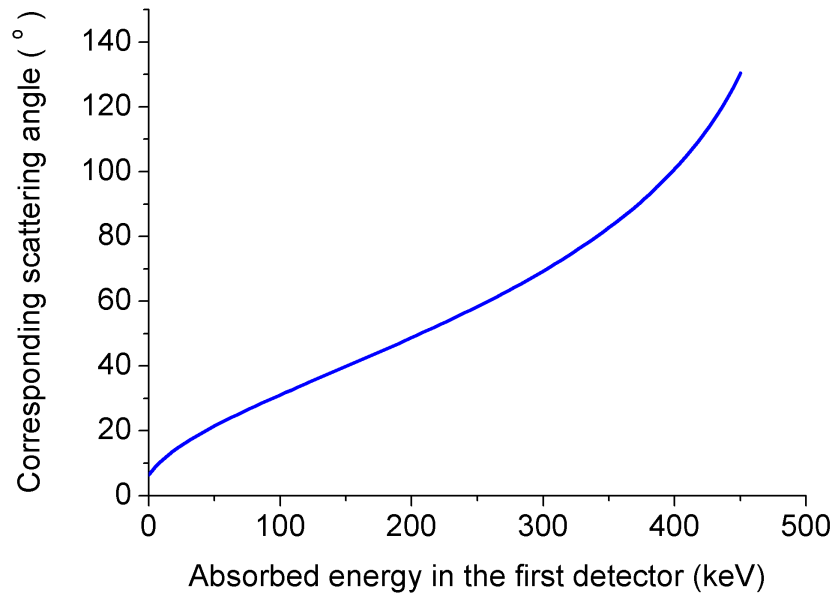


Figure 22: The correlation between the scattering angle and the released energy.

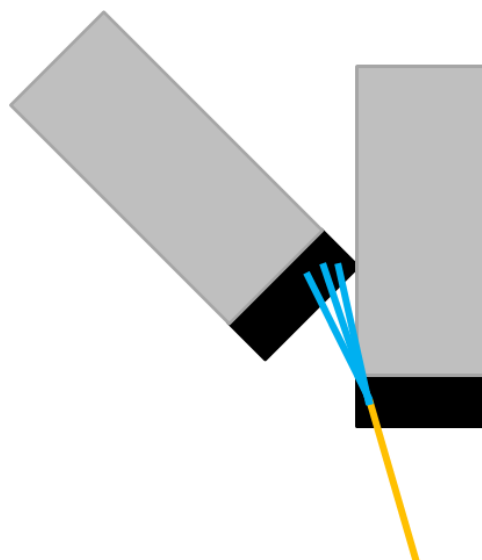


Figure 23: Photons scattering in small angle. The same side of the first detector is affected the most by the own activity of the absorber detector.

3 Simulation and reconstruction

In order to simulate the behavior of the detector signals we wrote a Monte Carlo simulation software in C. With the help of this simulation program the probability matrix for image construction can be easily done as well. In this section these two code is described.

3.1 Monte Carlo simulation for Compton camera

In the literature of Compton camera, the majority of the papers deal with energies under 600 keV. The reason of it is that the main applications for this configuration is nuclear medicine where the typical energies are 140.5 keV (Tc^{99m}), 364 keV (I^{131}), 93 keV, 85 keV, 300 keV (Ga^{67}), 511 keV (PET). In contrary, during prompt gamma activation higher energies should be handled. Therefore for deeper investigation of the features of the Compton camera concept, we made a Monte Carlo (MC) simulation software. The first version of the simulation was made in MatLab. But it seemed to be too slow for our purposes. Thus the remaking of it in C improved the speed.

Originally it was created for optimizing the detector geometry and material and preliminary optimizations for Si strip detectors were carried out. Though in extent these efforts were considerable it is not included here as the final experimental part concerned a different sort and thus different modeling. Meanwhile it cleared up that the main purpose of the program will be the generation of the probability response function (3.3.2 section). The constituents of the system can be defined as a box shaped source and two detector crystals. The detectors can be rotated freely around one fixed direction parallel with one of their edges. Hereinafter, this direction will be the direction of the x axis. Both the source and the detectors can be placed anywhere. The number of the detectors is variable. For the basic Compton camera two detectors are enough, but for larger energies the spatial resolution can be improved by two scattering detector [SKP⁺10]. A following thesis can include the examination of this opportunity as well.

3.1.1 Simulation algorithm

Generally every computational algorithm is called Monte Carlo method which based on repeated random sampling and the calculation of result as the average of the outputs. This can be used for simulate particle transport as well [LK90]. Here a brief overview is provided about the standard algorithm of a MC gamma transport simulation.

As a first step a photon released from the source volume's random point. Its initial direction is drawn isotropically from that solid angle range which contains the first crystal volume. Then the photon's propagation in the detectors' material and their interactions

are followed up until the photon has an energy higher than zero and stays inside the geometry set-up. At the beginning of its life and after each interaction a dimensionless path length is drawn: $r = -\ln(\xi)$, where ξ is a uniformly chosen number between 0 and 1. It can be converted to real length with $l = \frac{r}{\Sigma_{tot} * \rho}$ equation, where Σ_{tot} is the total mass attenuation coefficient of the detector material on a certain energy and ρ is the density of the matter. Between two interactions (including the birth of the photon as well) the program always look for the closest detector face in the way of the photon. If the dimensionless path is long enough to pay the distance until this surface, then the photon is transported there then the next closest face is under search. Otherwise the photon is moved to that point where the r becomes zero and the selection of the interaction type occurs. It can be Compton scattering or photoabsorption or pair production. Their probability is defined by the ratio of the process's linear attenuation coefficient and the total attenuation. If during the interaction the photon does not lose all of its energy, the process continues from the path length drawing step. The control flow graph is demonstrated on Figure 24.

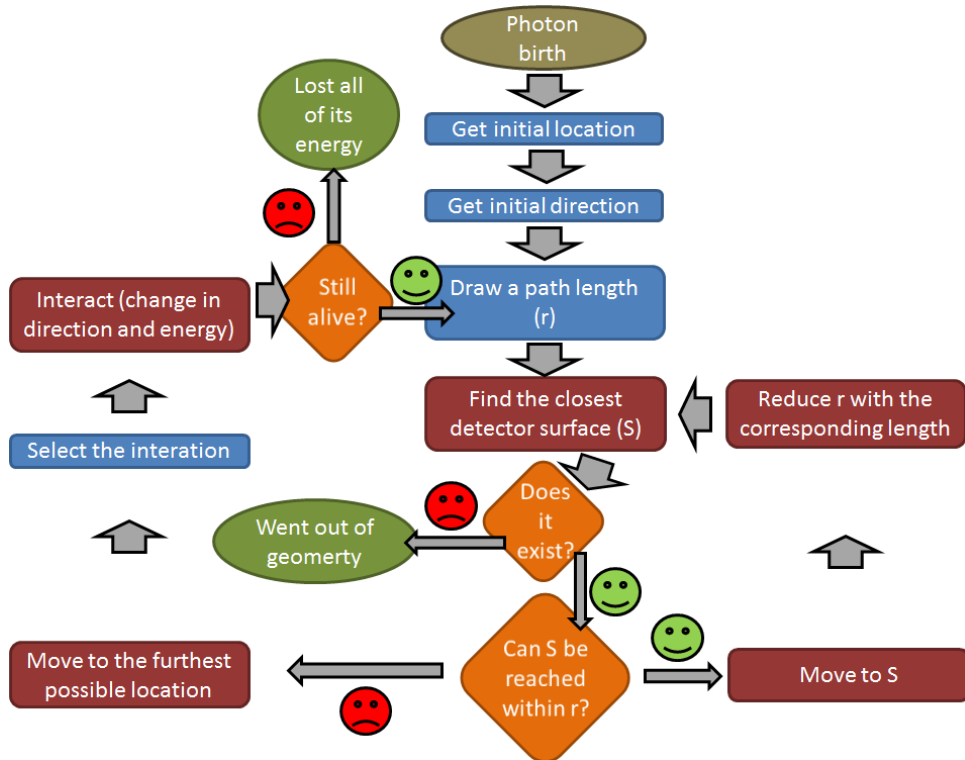


Figure 24: Control flow graph of the simulation program. Meaning of the bubble's colors: green: initial or final state, blue: requires a drawing, red: calculation step, orange: decision making

The program can provide different time of outputs. Due to its original purpose it can give back for instance the valid photon detection efficiency that quantifies the detector geometry's availability for Compton camera. A photon counts as valid if its first inter-

action is a Compton scattering in the first detector and the second (and the last one at the same time) is a photoabsorption. So the valid photon detection efficiency means the number of the valid photons divided by the total number of simulated photons. Including multi-scattering in the first detector can be taken into consideration as well in further investigations [Nag06].

Another output option is a list about the details (location, absorbed energy, type of interaction) of all of the interactions taken place in the detectors. A variation of it is to simulate the exact working process of a realistic detector. In a real measurement, a detector cannot make a difference between two interaction caused by the same photon almost simultaneously. Only an average signal can be obtained. The model of this complex signal can be described with the following formulas:

$$x^{(j)} = \frac{\sum_{i=1}^{N^{(j)}} X_i^{(j)} \cdot E_i}{\sum_{i=1}^{N^{(j)}} E_i}, \quad y^{(j)} = \frac{\sum_{i=1}^N Y_i^{(j)} \cdot E_i}{\sum_{i=1}^N E_i} \quad (6)$$

Where $x^{(j)}$ and $y^{(j)}$ indicate the interaction coordinates got from the detector thanks to its averaging tendency. $X_i^{(j)}$ and $Y_i^{(j)}$ are the coordinates of the central point of the j th detector's pixel where the i th interaction of the given photon occurred. N is the total number of interactions in the j th detector ($j = 1$ or 2). E_i is the absorbed energy during the i th interaction. This formalization is easy to conduct with a computer program. And the result can be used as an ideal input for image reconstruction as it was done in our case as well. For more details see section 4.1.

The third type of the available outputs is generated in order to make the program comparable with other MC simulation programs. It calculates the pulse height energy spectrum and the flux's energy spectrum in each detector. This method is detailed in the next section (3.1.2)

3.1.2 Comparison with MCNP simulation

In order to validate the appropriate functioning of my program, it was necessary to compare its result with a creditable simulation software result. The choice was the MCNP [LAB08]. However its handicap is the lack of the ability to handle coincidence events. The common points on which a comparison can be based on are the energy spectra. Two types of them were used. The first is the pulse height energy spectrum that has the F8 notation at MCNP. It indicates the energy distribution of pulses created in a detector [LAB08]. The second one is based on the calculation of flux over a volume (F4 tally at MCNP). More accurately the energy distribution of the track length estimated volumetric

flux.

$$\Phi = \frac{\sum_i l_i}{V} \quad (7)$$

Here Φ means the particle flux, l_i the passed length after the i th interaction and V is the detector volume. In practice when the photon is moved inside the detector material, the value of the energy bin belonged to the photon's current energy is increased by the length taken. After collecting the data from each simulated photons, the energy spectrum is divided by the volume of the detector.

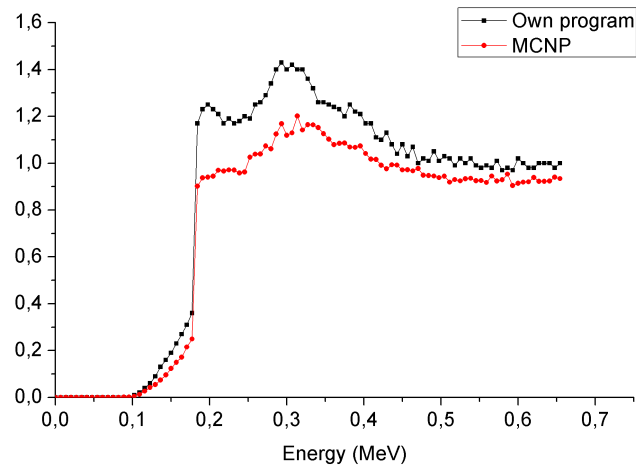
In the comparison the same number of energy bins was set. The material of the detectors in one simulation were the same. Once LYSO, then silicon. The source energy was 661.7 keV (the $Cs - 137$ γ -energy). The initial direction of the photons restricted to one direction, which is perpendicular to the first detector's front face (and parallel with z axis: $[0,0,1]$). To simplify the geometry the two detectors were only placed after each other with parallel positioning, thus no rotation was applied. The distance between the two detectors was 1cm. The size of the detectors is $5 \times 5 \times 1.2 \text{ cm}^3$. The result is shown on Figure 25(a).

The differences between the two flux and two energy spectrum curves are within 10%.

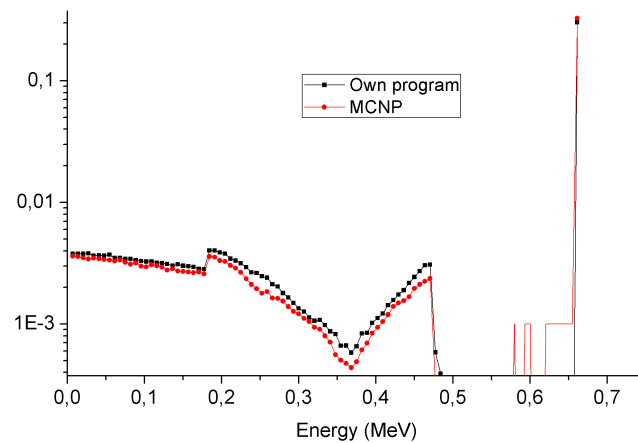
Since our major interest was the Compton scattering we examined the features of the flux spectra connected to scattering. If there is even a slightly difference between the cross section libraries used by our software and by MCNP, after several Compton scattering the error can increase due to error propagation. This effect is expected at lower energy ranges in the case of flux spectrum and higher energy ranges at pulse height energy spectrum. Look at the figures from this point of view, at smaller energies (<0.4 MeV) this error increases indeed in the case of flux. However the difference stays below 20% here also. In the case of silicon detectors, the difference is more significant. It supports the idea that the the key of the explanation is based on the multi-scattering. To go after this a few other tests were conducted.

Those length contributions of the total flux were separated which arise before the first interaction of the photon. These are the pathes taken by the photon before it is totally absorbed directly after its birth or before its first Compton scattering or before it escapes the detector volume. This restriction can be set with the help of FTn INC and FUn cards in MCNP. There should be only one non-empty bin, the bin corresponding to the energy of the source. The reason for it is that before its first interaction the photon does not lose energy, so it keeps its original energy. So this single value was compared in the case of the two simulation and it is found to be equal within 0.5%. Therefore it can be claimed that the reason of the difference is not the path length drawing.

Next probe was the increment of the material density in the case of the Si. With this



(a) Flux energy spectrum. Above 0.4 MeV the difference is < 10%, but below 0.4 MeV it is only < 20% due to the different cross section libraries.



(b) Pulse height energy spectrum. The bigger differences appear here at higher energies also because of the different cross section libraries.

Figure 25: Compton camera simulation with two LYSO crystal by MCNP and my own C program

modification less photon can escape without or just with one scattering, so there should be more multi-scattering. The result of it supports our clue. In the case of more dense detectors, the difference between the two flux curves grows. Especially at the energies below 200 keV. Above it the difference is negligible. Of course, because the higher energy bins refer to the photon life sections before the first or maximum before the second interaction (scattering or absorption).

As a conclusion we can say, that the seen alteration is thanks to lots of small energies absorbed during multiple scattering, because my cross section library is not as fine in energies as the one used by MCNP. In the case of several scattering interactions, even a small difference can cause a spread out phenomena through error propagation. Hence these differences are not significant, we accepted the performance of the simulation software.

3.1.3 Optimization

As it was mentioned before, the main purpose of the simulation code was to optimize the parameters of the detector positioning. These can be the material, the thickness, the size, the angle and the distance between the two detectors and the source. This section is only a demonstration of the opportunity to use the simulation software for this kind of optimization applications, since as it will be described later the limitation of our detector system at the moment is not caused by wrongly chosen geometry parameters.

Distance between detectors

For now, the index of the goodness was the proportion of the photons that endured exactly one Compton scattering in the first detector and directly after a photoabsorption in the other one. These pathways are the useful ones in the point of view of a Compton camera. Figure 26 shows the result of a possible optimization task. There are two LYSO crystals parallelly placed after each other. The distance between their central point is 1.5 cm and from the source 1 cm (the 1st one) and 2.5 cm. The two middle point and the point source lay on one line. The dimension of the detectors: $5 \times 5 \times d$ cm³ and $5 \times 5 \times 1$ cm³, where d is the variable waiting for optimization.

There is two contrary process that influence the result. With increasing thickness the probability of interaction is increasing, so there is bigger chance for Compton scattering. But with increasing probability of scattering, the chance for absorption moves together, thus a photoabsorption after a scattering in the same detector keeps the photon from arriving to the second detector. The figure fulfills our expectations. An optimal scatterer thickness exists in this configuration and it is $d = 1.25$ cm. One can say that the difference is only due to the statistical error. So let us assume the relative standard deviation for the efficiency! Equation 9 illustrates the square of the relative error of the measured

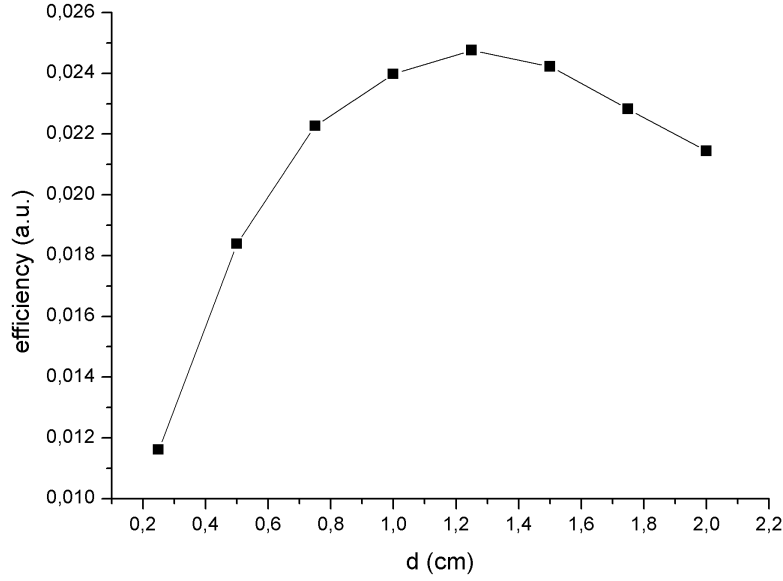


Figure 26: Optimization of the thickness of the scatter detector.

quantity I:

$$I = \frac{1}{N} \sum_i^N \omega_i \cdot d(x_i), \quad (8)$$

where N is the number of simulated photons, ω_i is the weight of the i th photon and $d(x_i)$ is the detector function. In our case, since I used analogue capture $\omega_i = 1$ and

$$d(x_i) = \begin{cases} 1 & , \text{if the photon has a valid path} \\ 0 & , \text{otherwise.} \end{cases}$$

$$r^2 = \frac{D^2(I)}{I^2} = \frac{\sum_i^N \xi_i^2}{\left(\sum_i^N \xi_i\right)^2} - \frac{1}{N}, \quad \xi_i = d(x_i) \cdot \omega_i \quad (9)$$

If η is the efficiency and M is the number of valid photon paths, then $M = \eta \cdot N$. From this:

$$r = \sqrt{\frac{1}{M} - \frac{1}{N}} = \frac{1}{\sqrt{N}} \sqrt{\frac{1}{\eta} - 1}$$

With $\eta \approx 0.02$ we can calculate $r = 0.7\%$. Therefore the values on the figure differ beyond the their errors.

Inclination angle Above an example was shown as an application of the simulation program. This type of calculation cannot be accomplished or pretty tricky to do it with

MCNP since the only way to get list mode information about the interactions is the so-called ptrac (Particle Track Output) card [LAB08]. But in our case a lot of parameter is given, they are not optional. This concerns for example the detector material and the thickness. So examining a more realistic set-up, opting the inclination of the detectors. The angle between them already determinate the distance of their center. Thus a good question emerge: Is there such like optimal angle between the two detectors alignment? If yes, what is it? However in the experiments detailed in section 2.3.1 and 4 are not based on this type of optimization. The angles there rather came from the consideration of the scattering angle of the chosen material and the angular resolution caused by finite energy resolution. In the future, the software optimization can be added to these aspects to tune the detector configuration and the used phantom. Here only for demonstration the efficiency is calculated for a few angles. The result can be seen in Table 3. The distance between the two detectors middle point was calculated from the θ angle. θ is defined by the angle between the principle axis of the first detector and the line connecting the two central point (see Figure 27).

angle($^{\circ}$)	D (cm)	η
30	11.3	0.001261
45	7.5	0.002137
60	5.5	0.002317

Table 3: Detector configuration efficiency in the case of using a couple of different angles of inclination.

However it is less likely that a photon with 661.6 keV energy scattering in 60° than in 45° , the second detector can be placed closer in the first case, so less photon can escaped from the geometry between the two detectors. According to the table, the effect of distance is stronger than the effect from the angle probabilities. I also have to add that of course with a θ - configuration not only those photons are detected that have been scattered exactly with θ , but the ones changed direction in a wider angular interval.

However, above a few examples were shown for geometry optimization, in the case of a real measurement we did not have freedom to vary every geometry parameters. As it will be concluded in the section 4, the goodness index of interest describing a geometry configuration is not the detection efficiency. The achievable resolution of the reconstructed image is a better parameter.

3.2 Data storage

The data coming from an experiment is expected to be in a list. Every element of the list consists of the parameters of two events happened in the same time (within

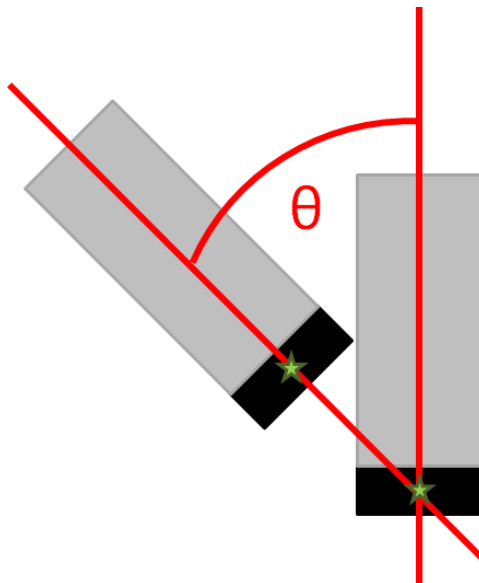


Figure 27: Definition of θ as the angle of inclination between the two detectors. Black color indicates the LYSO crystals, the green stars mark the center of the detectors.

the coincidence time window). These parameters are the x and y positions and the absorbed energies (in the first detector for the first event and in the second detector for the second event). The positions and the energies are both stored in discrete values. The 256x265 position bins correspond to the 5x5cm detector surface. The meaning of the energy bins can be found out with energy calibration (see section 2.3.2). The bins are always represented with their middle values. It was already shown in section 2.3.5 that the coincidence pairs' filtering for their total absorbed energy has an utmost importance. Considering the energy resolution, a relatively wide window should be set for this purpose: $[E_0 - 100 \text{ keV}, E_0 + 100 \text{ keV}]$, where in the case of cesium source $E_0 = 661.7 \text{ keV}$. In the case of a single examined source energy this goes hand in hand with a simplification of the used data set. The second absorbed energy can be skipped. Thanks to the discrete values, there is a finite number of possible x-y-energy structure. Thus, a sole index can be used for their description. The identity number of this detection bin can be constructed in the following way:

$$I(x_i^{(1)}, y_j^{(1)}, e_k^{(1)}, x_m^{(2)}, y_n^{(2)}) = i + x_{max}^{(1)} * (j + y_{max}^{(1)} * (m + x_{max}^{(2)} * (n + y_{max}^{(2)} * k))),$$

where x_i, y_j are the i th and j th position bins, e_k is the k th energy channel, $i, j, m, n = 0, \dots, N - 1, k = 0, \dots, N_E - 1, N$ is the number of pixels in one direction (above: $x_{max}^{(1)}, x_{max}^{(2)}, y_{max}^{(1)}, y_{max}^{(2)}$) and N_E is the number of energy channels. Or introducing the detector

pixel indices: $p_a^{(1)} = i + x_{max}^{(1)} * j$, and $p_b^{(2)} = m + x_{max}^{(2)} * n$, where $a, b = 0, \dots, N^2 - 1$.

$$I(p_a, p_b, e_k) = a + N^2 * (b + N^2 * k), \text{ where } I = 0, \dots, M$$

To sum it up, actually the image reconstruction's input is an array - let us note it with $\bar{y} = [y_1, \dots, y_M]$ -, whose elements store the number of the coincidence events that correspond to that certain detection bin. The required output is an array as well that denotes the source intensity of the voxels of the object. This will be $\bar{x} = [x_1, \dots, x_S]$.

3.3 Image reconstruction

In the previous chapter the validation of a MC simulation software was already successfully done. Partially based on that code, an image reconstruction software was written. This section demonstrate what features make it applicable for our purposes. The requirements that it fulfills are listed below:

- Have the ability to process the data directly coming from the data acquisition software.
- Several parameters can be chosen freely: Source energy, inclination and position of the detectors, distance between the detectors, number of pixels of the detectors and number of voxels of the object.

The task of the image reconstruction program is to provide \bar{x} from \bar{y} . It can be written in a form of linear transformation: $\bar{x} = A\bar{y}$, where A is the system response matrix with $S \times M$ dimension. A_{ij} element is the probability that a photon emitted in image voxel j is detected in measurement bin i .

From the concept of the Compton camera configuration the simple backprojection can be deduced: From the positions of the two paired events, and the released energies the angle of scattering can be calculated, so there is a conical surface on which the photon could originate. From the intersection of these cones, the source object can be reconstructed.

Another approach is the maximum likelihood (ML) method. It is based on the maximization of the so-called likelihood function which is a conditional probability density function: $L = \mathbb{P}(\bar{y}|\bar{x})$, where \bar{x} is the parameter array and \bar{y} is the random variable. The method gives an estimate for the most likely parameter set that could have caused the measure values of \bar{y} . The formalization of it reads:

$$\hat{\bar{x}} = \underset{\bar{x}}{\operatorname{argmax}} \left\{ \ln [\mathbb{P}(\bar{y}|\bar{x})] \right\}$$

This technique can be extended with an iterative solving method, called expectation maximization (EM) detailed below.

3.3.1 ML - EM method

The key of it is the assumption that \bar{y} measured data can be completed to a complete s_{ij} system, where s_{ij} is the number of the photons emitted in the j th object voxel and detected in the i th detection bin. Its connection with the measured data is

$$\bar{y}_i = \sum_{j=1}^M s_{ij} \quad (10)$$

One iteration step has two main substeps:

1. Expectation - Expected value calculation

$$Q(\bar{x}, \hat{x}^{(n)}) = \mathbb{E} \left\{ \ln \left(\mathbb{P}(s|\bar{x}) \mid \bar{y}, \hat{x}^{(n)} \right) \right\} \quad (11)$$

2. Maximization - Standard ML execution

$$\hat{x}^{(n+1)} = \underset{\bar{x}}{\operatorname{argmax}} \left\{ Q(\bar{x}, \hat{x}^{(n)}) \right\} \quad (12)$$

It can be shown [Orv], that

$$\ln(\mathbb{P}(y, x^{n+1})) - \ln(\mathbb{P}(y, x^n)) \geq 0.$$

With other words performing one iteration step the probability that the sampling of \bar{y} was done with the \bar{x} parameter set at least do not decreasing.

After the general introduction let us see a specific case of interest. In the case of Compton camera, the number of photons reached the j th detection bin shows a Poisson distribution:

$$\mathbb{P}(\bar{y}_j) = \frac{[\mathbb{E}(y_j)]^{y_j} \cdot e^{-\mathbb{E}(y_j)}}{y_j!}$$

From Equation 10

$$\mathbb{E}(s_{ij}) = A_{ij}x_j$$

Following the two-step recipe described above with filling in these expression one can get the next equation for one iteration step:

$$x_j^{(n+1)} = x_j^{(n)} \frac{1}{\sum_i A_{ij}} \frac{\sum_i A_{ij} y_i}{\sum_m A_{im} x_m^{(n)}} \quad (13)$$

So finally, the ML-EM method is simplified for an iterative linear equation solver.

3.3.2 System response matrix

The only missing piece now is the probability response matrix. A_{ij} is the probability that a photon emitted in the j th voxel of the object detected in the i th measurement bin. Since there is already a MC simulation program at hand, it is practical to calculate the probabilities with it.

For a given geometry (object, detectors positioning, inclination), from every voxel of the object the same number of photons were started isotropically (spatially and angularly) with the same energy. Then the number of photons arrived in the detection bins was counted for every starting voxel separately. To get probabilities, at the end a division by the number of simulated photons are required. Unfortunately, a matrix correspond to only one fixed geometry, so for different experiments it has to be calculated again. In ideal case, when the detectors have 33x33 and 35x35 pixels per each, and the number of energy bins are 20, $2 \cdot 10^7$ measurement bins belong to each voxel. The calculation speed of the software on the best available processors at our disposal was 10^6 particles / s. Furthermore, even with detectors containing 20x20 pixels the memory requirement of the *double* variable matrix for each object voxel would be 160 Mbytes. So without dedicated hardware or specially designed algorithms the calculation of this ideal matrix cannot be the part of this work (With the 20x20 pixels and 20 energy bins it would last for 1 year). Therefore restrictions in bin numbers were applied. From the estimation mentioned in section 2.3.1 in order to be able to distinguish the two side of an $4 \times 4 \times 4 \text{ cm}^3$ object the energy resolution should be lower than 150 keV. With the hope that we can get a little bit more detailed reconstructed image than this, the number of the energy bins were set to 20 yielding energy bins of width 12.5 and 20 keV. The detected range of the absorbed energies are 250, 400 keV. It comes from an estimation as well detailed in the same section.

4 Experimental setups

After preliminary investigation of convenient gamma-detection and the theory of the image reconstruction engine the experiences were applied in practice with success. Projections from one simulated and from two real measurements were reconstructed by our own software. The results are discussed below.

4.1 Virtual and real $Cs - 137$ source

4.1.1 Test of the reconstruction engine

The stability of the ML-EM iteration convergence is not obvious. It can be too stable or instable depending whether the equations are over- or underdetermined. Thus, in order to test the stable convergence produced by our image reconstruction software, a simplified system was defined and used for this aim. Even the input data for the reconstruction was a simulated not a real one to eliminate disturbing effects. This test system constructed from detectors with 4x4 pixels and 20 energy bins on the 0 – 200 keV energy range. The source was at an off-center position (at the voxel (1,2)). Its distance from the first detector's front face was 1 cm. The number of the emitted particles was 10^7 . From efficiency calculations (section 3.1.3) we concluded that around one photon from 500 has useful coincidence events. If we have an aim to get 100 particles in the detection bins which are most likely, the relative error can be kept under 10%. Starting $1.6 \cdot 10^9$ photons from the chosen off-center voxel, scores were about 500 in each important bins. A two dimensional image was created forming a set of identical cubes in a 4x4 raster. The convergence of the intensity in the 16 voxels and the reconstructed image are shown in Figure 28. It is clear that the convergence is stable. The intensity of the required voxel converges with a satisfying degree. Only the neighbor pixels ((1,3), (1,1), (2,2)) converge slower than the other, which is a normal tendency.

4.1.2 Testing imaging capabilities

For further analysis of the reconstruction program capabilities the same simplification trick was used. Namely to simulate the measurement data using a virtual $Cs - 137$ source. The detector configuration is the usual asymmetric one: the second detector is rotated with 45° . Voxels were cubes of 0.2cm of side length organized in a 20x20 raster parallel to the first detector's frontal surface. The number of energy bins is left the same as above, but the detector's spatial resolution was improved by using 10x10 pixel division. $2 \cdot 10^9$ particles were used for the system response matrix generation, which resulted in $9 \cdot 10^7$ coincidence events under 45 hours of calculation time.

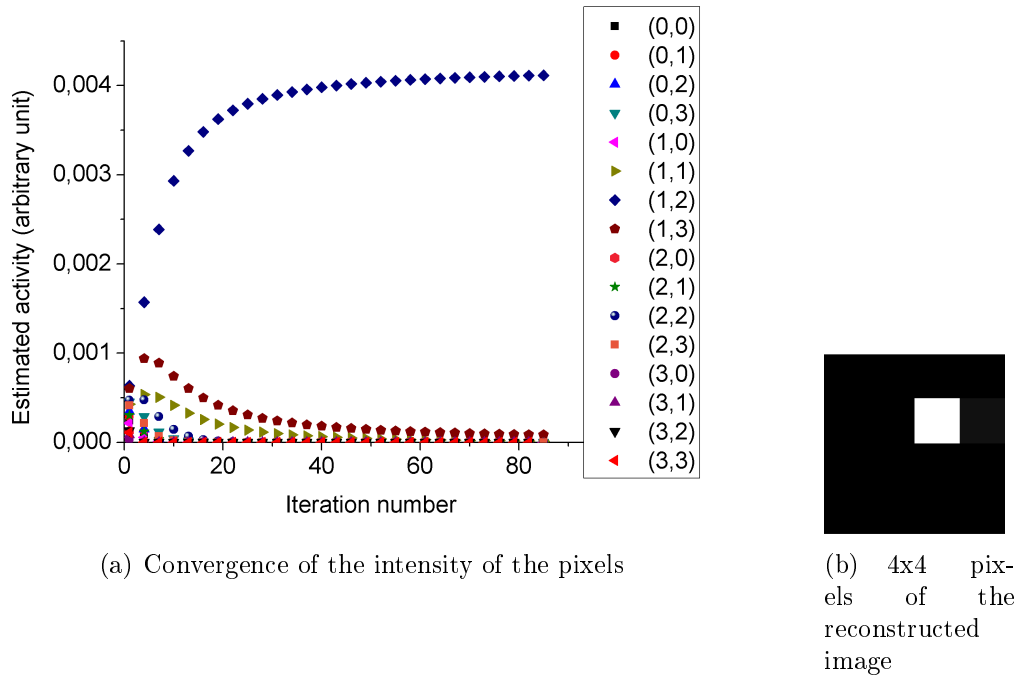


Figure 28: Result of the image reconstruction test

Three data sets were generated, each has the source voxel in different position: upper-right (15,15), exact center (10,10) and lower-left (5,5). The received images after the 23th iteration are demonstrated on Figure 29.

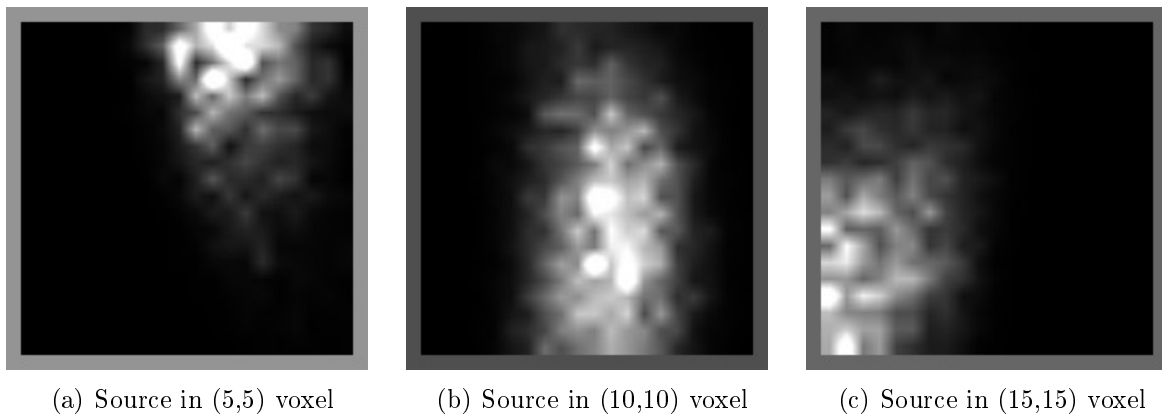


Figure 29: Reconstructed images of three point sources placed in different voxels. The vertical resolution is far below the horizontal one

The first evident characteristics is that the spatial resolution in the two directions differ significantly. It was an expectable feature since in the horizontal direction the detectable range of the scattering angle is spread out from 0 to 90 degrees resulting in high horizontal resolution. The interval of the detected angles in the vertical direction

is significantly narrower, only a few-degree-wide that means low vertical resolution. An illustration of the maximal scattering angles can be found in Figure 30. Therefore we can state that the reconstruction with the current set-up at a single projection angle is rather in 1D than in 2D.

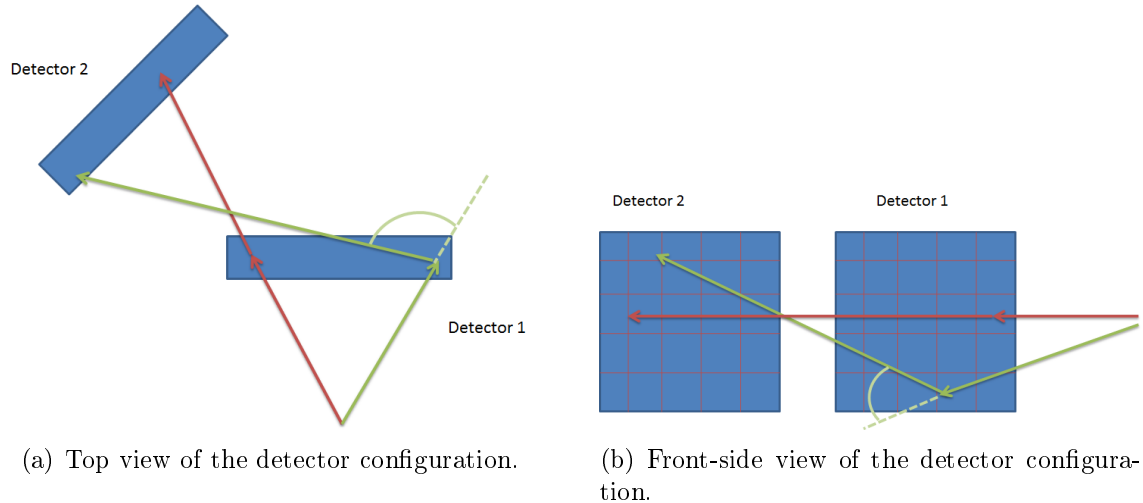


Figure 30: Illustration for the anisotropy of the resolution.

The next major characteristic is that the reconstructed images especially for the off-centered sources tend to be "attracted" by border voxels, i.e. the side pixels are enlighten more than they supposed to be. This effect is often seen in ML-EM reconstructions.

The last observation that is worth to mention is that the reconstruction is not smooth but forms "blotches" indicating a poorly calculated system matrix.

4.1.3 Measured data image reconstruction

We already discussed a measurement with Cesium source in section 2.3.5 regarding the correlation between the first released energy and the scattering angle. The same measurement can be used to demonstrate the features of the reconstruction algorithm on a realistic data. Here only the result of a 2 dimensional (actually rather 1 dimensional) reconstruction is shown. However with a faster software or with more available time multiplying the same data can be used as a tomography data series: several projections of the point source from different angles. The geometry is exactly the same as at the previous section (10 cm first detector - source distance, 45° inclination), so the same probability response matrix can be use which has been already calculated. The reconstructed images can be seen in Figure 31. The raw data (Fig. 31(a)) has been affected by highlighted corner and edge effects. This type of phenomena was observed in the case of simulated data as well. Figure (b) and (c) was made from data with more strict restricted total

absorbed energy windows and pixel cut-offs. The parameters of the three attempts are the followings:

- (a) Sum of released energy should fall within $662\text{keV} \pm 250\text{ keV}$: image contrast and brightness were adjusted until vertical line became visible.
- (b) Sum of released energy should fall within $662\text{keV} \pm 100\text{ keV}$ and a 2 (out of 10) wide-detector pixel edge was cut off at the edges of both detectors, image contrast and brightness were adjusted until vertical line became visible.
- (c) Sum of released energy should fall within $662\text{keV} \pm 100\text{ keV}$ and a 3 (out of 10) pixel-wide detector pixel edge was cut off at the edges of both detectors, image contrast and brightness were not adjusted, since vertical line was already visible.

The typical characteristics of the previous reconstruction attempts appeared here as well. With proper preprocess of the data the resolution of the image can be improved significantly. The useful recipe was to eliminate the misbehaving data, so with more data tailoring it is expected that the resolution can be refined on.

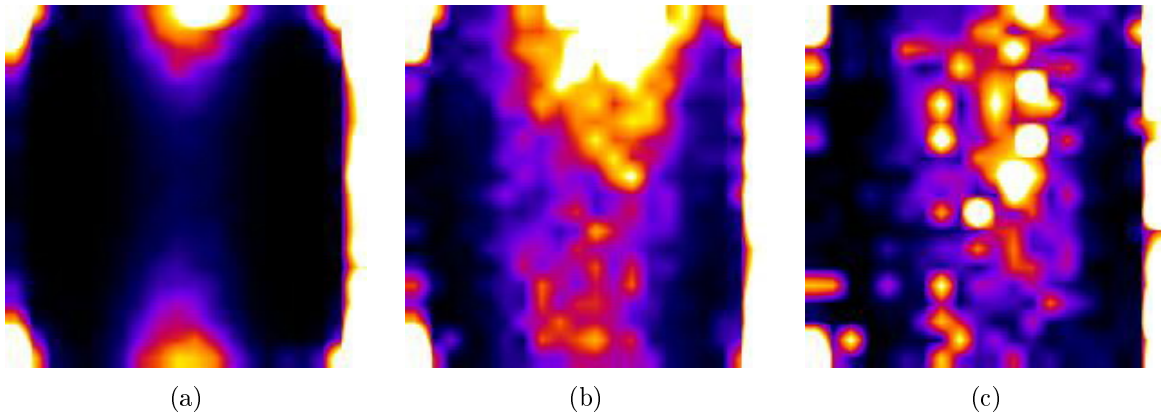


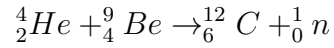
Figure 31: Cs point source reconstructions using different data filtering increasing restrictions from (a) to (c): image quality improves.

4.2 Neutron sources

As we showed in the previous section, the image reconstruction of a projection made from a γ -ray point source with Compton camera configuration can be done successfully. Thus we can take the next step in order to show the possibility of using this imaging system for PGAA: prompt-gamma production with a neutron source instead of the formerly used γ -source. In our case there were three possibilities for the neutron source type: isotropic neutron source, neutron generator and nuclear reactor.

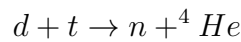
4.2.1 Options

The tried isotopic neutron source was Plutonium-Beryllium (PuBe). The neutron production function of the PuBe source based on an (α, n) reaction. Plutonium is the alpha emitter, which is mixed together with the Beryllium as a powder. The neutron is gained from the following reaction:



The emitted neutrons leave the source with a continuous energy spectrum that is dependent upon the energy of the alpha particle. The average neutron energy is 4.5 MeV.

Another possibility was the DT (Deuterium-Tritium) neutron generator. It is one of the most common acceleration-based neutron source. Creating Deuterium ions and accelerating these ions into a Tritium target produces neutrons. Deuterium atoms in the beam fuse with Tritium atoms in the target to produce neutrons.



The energy of the neutrons is uniformly 14.2 MeV.

The third neutron source type to mention is the most complex one, the nuclear reactor. During the sustained nuclear chain reaction a heavy nucleus splits into two or more lighter nuclei, while it releases gamma radiation and free neutrons.

4.2.2 Comparison

The features a convenient neutron source need to show regarding its use for PGAA are listed below:

1. **Neutron flux.** Quantifying the number of neutrons available at a certain position. The associated energy spectrum of the flux must also be known for quantifying the (n, γ) reactions to be expected.
2. **Ease of its use.** Electricity requirements, authorization requirements, length of preparation time, mobility, ...
3. **Availability.** In the case of nuclear reactors it refers for example to the available beam time. Or in the case of the neutron generator the end of authorization procedure within the required time.
4. **Neutron energy range.** In the point of view of a required simulation the more accurate estimations can be done for the neutron source with known energy spectrum.

The easiest way to meet with this demand is to have only one energy level.

5. **Background gamma radiation.** During the operation of the source it shall not produce other particles, just neutrons. Considering especially the γ -photons, which can disturb the detection of the prompt- γ -s.

A summary whether the available neutron sources fulfill these points is shown in Table 4.

	Flux (num/ s/cm ²)	Ease of use	Availability in time	Energy spectrum	Back- ground
PuBe	Really low	Easy	+	Broad	High γ
DT neutron generator	10^7	Need of authorization	-	Monoenergetic (14.2 MeV)	Low
NTI Training reactor	$6 \cdot 10^4$	Fixed, beam time	+	Broad	High γ
Cold Neutron Source	$3 \cdot 10^7$	Fixed, beam time	+	Ultra cold (<5meV)	Low

Table 4: Comparison of neutron sources

The ideal choice from several points of view, would have been the neutron generator. Due to legislation issues within the available time access to it was not achieved. The operation of the neutron generator needs authorization, since it is an accelerator. The procedure of the permission would have been longer than the available time.

Thanks to its compactness we started the experiment series with PuBe source, but its neutron yield was so low, that the effects of the prompt- γ was not detectable.

Finally, the measurements were done with two different nuclear reactors:

1. Training reactor at Institute of Nuclear Techniques, Budapest University of Technology and Economics (BME)
2. Cold Neutron Source belonging to the research reactor of the Center of Energy Research, Hungarian Academy of Sciences

4.2.3 Sample selection

Achieving the maximal detection efficiency the used phantom material should be selected carefully as well. Table 5 shows a couple of materials that has high cross sections for neutron capture. Here the cross sections are thermal equivalent cross sections. These materials are the candidates for using them in a prompt-gamma neutron activation analysis, because they can give a signal that expected to be large enough to be detectable.

	Energy(keV) (σ (barn))
^1H	2223 (0.3326)
^{10}B	477.6 (716)
^{23}Na	470(0.53), 1368, 2754
^{27}Al	1779 (0.231)
^{35}Cl	517 (7.58), 1164 (8.91), 1951 (6.59)
^{137}Cs	176 (2.47), 205(1.56), 510 (1.54)

Table 5: Prompt gamma energies and thermal equivalent neutron cross section of a couple of materials (in brackets).

The aspects that have to be taken into consideration during the comparison are the followings:

1. The material should have a high tendency to produce prompt-gamma rays. That means large cross section.
2. Considering specifically our LYSO detector crystal's own emission it could be a big advantage, if the Compton plateau of the prompt-gamma energy goes either above 600 keV or stay below 300 keV.
3. For every source energy, there is an optimal scattering angle regarding the angular resolution (see section 2.3.1). The energy belonging to that angle should be above the energy resolution. For now it has less importance because the poor resolutions, but thinking about future developments it is worth to mention.

In order to make sure that we at least get a signal from any prompt-gamma we considered the first criteria as the utmost important one. This narrows the scale of the materials for boron and chlorine. To use them it is totally perfect to fill a sample holder with boric acid (H_3BO_3) and table salt (NaCl). This choice was a compromise, since the hopefully boron has a prompt-gamma energy at 477 keV, which is mixable with the photons coming from the LYSO. The chlorine has higher energy peaks at 1368 and 2752 keV, but its cross section lower with orders compared to the boron.

The sample holder was a polyethylene ($(\text{C}_2\text{H}_4)_n\text{H}_2$) cylinder with cylindric holes in it for the samples.

4.3 NTI Training Reactor

After excluding two possibilities for generating neutrons a series of experiments was conducted whether a horizontal channel of the NTI training reactor is convenient for our purposes.

4.3.1 Dosimetry calculations

The first attempt at one of the horizontal channel of NTI training reactor with the geometry and materials discussed in the previous chapters did not succeed. At that point, only one blocking system was eliminated from the two. The water was drained from the way of the neutron beam, but the iron plug was left in its own position. Unfortunately due to this the neutron flux was not high enough to produce convenient number of photons. We did not see any peak in the energy spectrum at the expected 477 keV, neither with a much larger NaI scintillation detector.

Removing the iron block seemed to be a solution for this. But dosimetrically it is a greater challenge, as data on the doses to be expected was not available. Subsequently a simulation was needed. For that purpose a modeling was conducted by MCNP5. The geometry model is demonstrated on Figure 32.

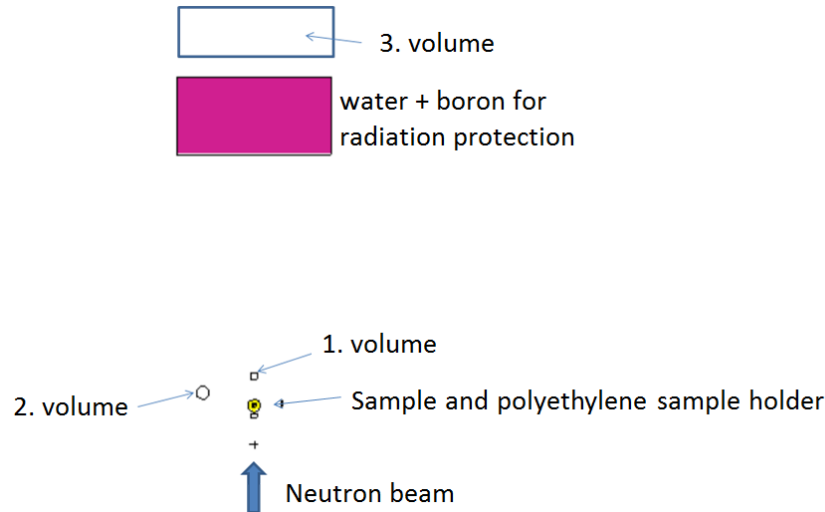


Figure 32: Geometry model for dose estimation by MCNP5. The three marked volumes are used for the absorbed dose calculations.

The available data was the following:

1. The neutron flux of the neutrons with an energy < 0.5 MeV at the reactor channel number 4 at 100kW power is $6.10 \cdot 10^6 \pm 10\% \frac{n}{cm^2s}$. For higher energy range it is $3.06 \cdot 10^6 \pm 35\% \frac{n}{cm^2s}$ [vZ06].
2. There was no available real measured neutron spectrum, so we used a simulated one from a zone model [KR].
3. The neutron dose rate in the neutron beam without water and iron blocking at 1 kW is $15 \frac{mSv}{h}$. For gamma ray the dose rate is approximately the double of it.
4. The boron concentration in the borated water filled dosimetry shields is 25g H_3BO_3 / 1 l water.

The sample holder was a polyethylene cylinder with 10 cm height and 5 cm diameter (Figure 35(a)). It was filled with boric acid and NaCl and placed in the neutron beam. The neutron beam is collimated and isotropic in space at the exit of the channel which is a circle with 12.5 cm radius. The used energy spectrum can be seen in Figure 33. The source spectrum and intensity can be calculated based on this spectrum and the flux given above. The gamma dose coming from the reactor was estimated as a three times larger dose than the calculated neutron dose. However the effect of the gamma rays produced during neutron activation are simulated, they contribution is negligible, since their maximal dose is lower than the tenth of the neutron dose.

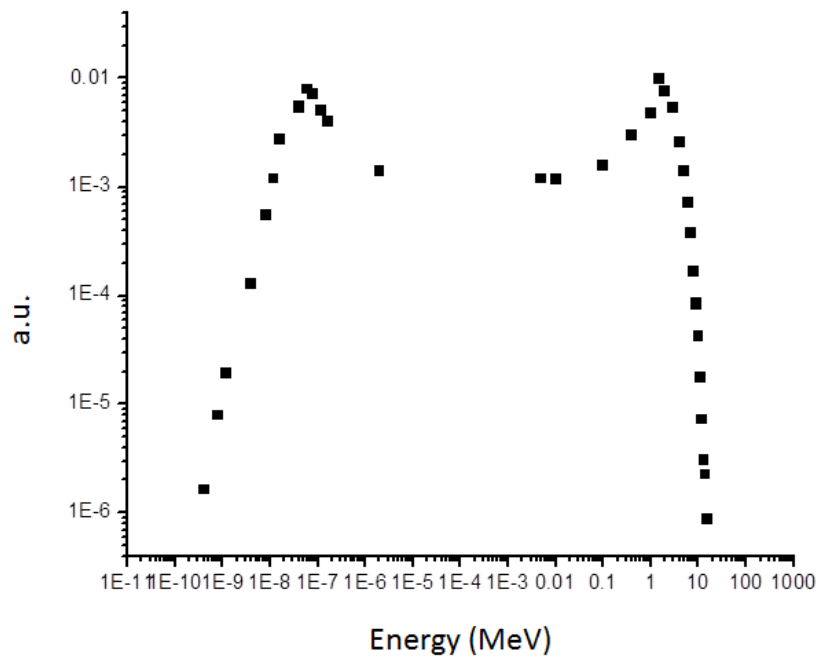


Figure 33: Simulated energy spectrum of the fast neutrons with MCNP5 based on zone modeling

The width of the boron shield was 80 cm, and its distance from the channel's exit was 3 m. The sample's distance from the exit was 0.5 m. The scatterer detector is placed at 20 cm from the sample. The dose was calculated at three different locations: After the sample, in the line of the neutron beam; after the sample, but off from the beam line ($\approx 30^\circ$ angle) and after the boron container. The dose can be calculated in two different ways. The first option is from the given neutron flux at the channel' mouth. Its result is reported in the second column of Table 6. The other possibility is to rescale the results in a way that the simulated dose would be the measured $15 \frac{mSv}{h}$ at 1kW power. The third column of the same table consists these results.

The conclusions are the following:

	Location	Scaling based on flux(mSv/h)	Scaling based on dose (mSv/h)
1. volume	Lined with neutron beam, after sample	4.68294	15.0
2. volume	Off the neutron beam, after sample	0.08954	0.28
3. volume	After the boron container	0.00144	0.00463

Table 6: Dose values at different locations

1. In the case of the doses scaled to the flux, the doses are underestimated. So in order to follow the conservative radiation protection principle, the doses scaled to the measured doses were accepted.
2. The dose contribution of the neutrons scattered on the sample is 2 % compared to the whole neutron beam.
3. The radiation protector with boron decrease the dose to $5 \frac{mSv}{h}$ at 1 kW. So the neutron dose rate behind the protection can be kept under $50 \frac{mSv}{h}$ at 10 kW. Due to the lack of the spectrum of gamma coming from the reactor channel, the gamma dose rate can not be estimated.

4.3.2 Simulation for detector signal

With the same simulation model a few more data can be gained. For example the number of photons coming in one second from the boron activation. It can be compared with the background coming from the LYSO.

In Figure 34 the pulse height energy spectrum of the scatter detector can be seen. The line between the detector and the sample center was perpendicular to the direction of the neutron beam. It is evident that the boron has significantly the biggest signal as it was expected. The peaks referring to chlorine also can be distinguished, but there is no trace of the hydrogen, oxygen or sodium.

According to the simulation, at 1 kW reactor power level the number of photons originated from the boron scattered in the first detector and absorbed in the second one is 7 / second. In the case of the $\theta = 45^\circ$ configuration and the 477 keV source energy, the released energy in the first detector is around 0 – 200 keV. Form this, the particle number mentioned before was estimated from the 300 – 500 keV range of the absorber detector's energy spectrum. From previous measurements the coincidence event's background from the LYSO own activity in the same energy range is 10 coincidence events in a second. It was really promising that with the power increment (10 kW) the useful signal would be a few times higher than the noise.

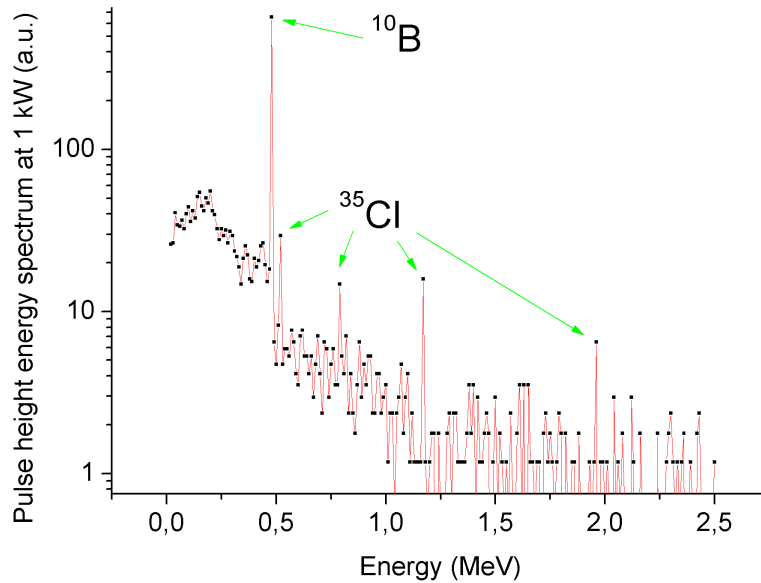


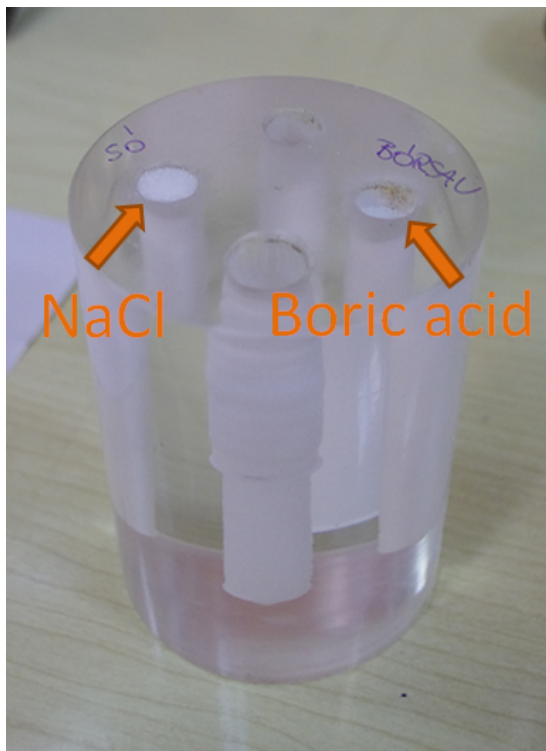
Figure 34: Simulated pulse height energy spectrum of PGAA with ^{10}B (H_3BO_3) and NaCl .

4.3.3 Results

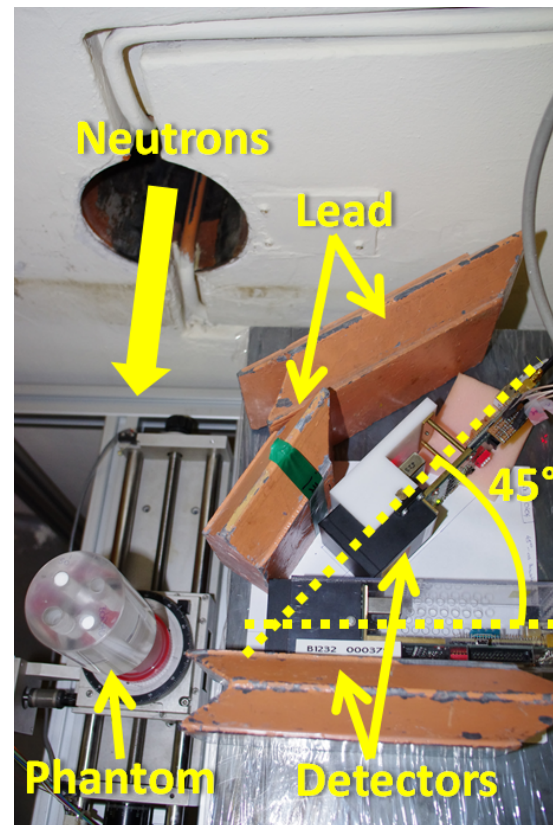
Following the considerations made above, the experiment without the water and the iron block was authorized. The power was increased gradually and both the neutron and the gamma dose were measured at different places of interest in the reactor hall (at the reception, in the beam and off the beam before and after the boron shield). The motivation of these measurement sites was to decide what is the maximal reactor power level that could be allowed without further safety procedures (e.g. partial evacuation of the reactor). The measured values for neutron doses were not in agreement with the ones from the MCNP simulation. At 8 kW the gamma dose was $1 \frac{\text{mSv}}{\text{h}}$ at the height of the beam outside of the boron shield. The neutron doses were negligible compared to the gamma doses.

Inside the protection wall, a NaI scintillator was in operation as well. As it was expected, a peak around 477 keV appeared on its spectrum. But on the spectrum a high background level formed coming from the reactor gamma background in the lower energy range. Regarding the dosimetric limitations the power increment was stopped at 8 kW. Our measurements were taken at this state. The modification in the geometry compared to the simulated one was the lead brick which was placed between the scatterer detector and the beam (see Figure 35(b)).

The high background at lower energies did not allow to get information about the Compton plateau in the scatter detector (Figure 36(a) and 36(b)). So the third neutron



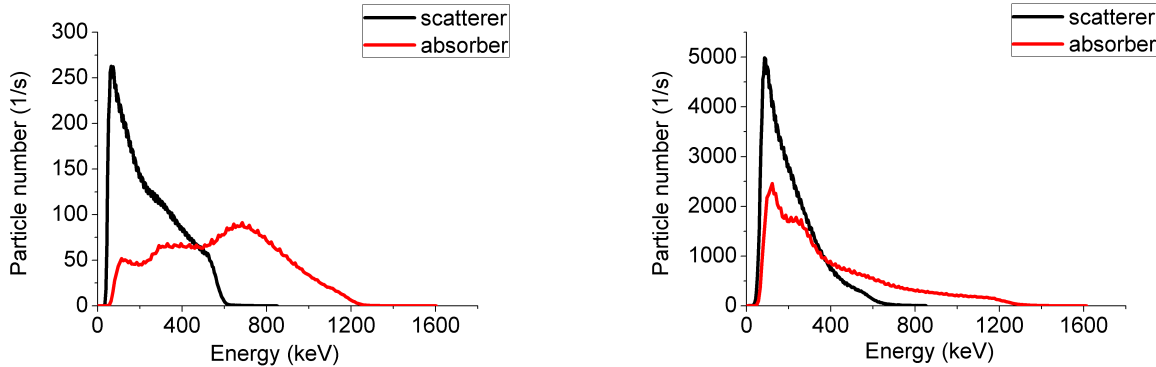
(a) Used phantom: polyethylene cylindric sample holder (5 cm diameter, 10 cm height) filled with boric acid and table salt.



(b) Experimental set-up at the horizontal channel Nr. 5 of NTI training reactor.

Figure 35:

source candidate has failed as well.



(a) At 100 W thermal power. At scatterer the own spectrum of the LYSO crystal is seen.

(b) At 8 kW thermal power. High low energy background.

Figure 36: Energy spectrum from the scatterer and absorber detectors.

4.4 KFKI Research Reactor

As the last available opportunity, we had a chance to make measurements in the Budapest Neutron Center (BNC). The reactor has a 10 MW maximum reactor power and ten horizontal beam tubes. At one of the tangential beam tubes a cold neutron source (CNS) has been installed. This is where our experiments took place.

4.4.1 Cold Neutron source

The main functional element of the cold neutron source is a special moderator cell filled with liquid hydrogen and placed at the end of the horizontal beam channel [GMR+97]. The volume of the hydrogen reservoir is 0.5 l filled with liquid of 14 K. From here the neutrons are led with neutron guides to the place of the measurement. Since the neutron as a particle has wave properties, it follows the same law for total reflection as light waves. The neutron mirrors are made of several hundred double layers of nickel-titan. The limiting angle for total reflection of a neutron mirror is much smaller than for light in the optical glass fiber. (For a neutron with 0.5 nm wavelength the limiting angle is approximately 0.5 degree.) Of course this angle is depending on the wavelength. The used neutron guide material reflects the neutrons with lower energies with higher efficiency, thus an energy selection is done as an extra cooling of the neutrons. Thanks to the really small total reflection angle, the collimation is done automatically as well. These special techniques result in a neutron beam that has a maximum energy of 0.5 meV. It is a big advantage in the point of view of PGAA, because the capture cross section for cold neutrons are 2-3 times larger than for thermal ones. Due to the bend of the guide the

neutron beam is not disturbed by γ -radiation or by fast neutrons, which is also a great advantage compared to the NTI training reactor.

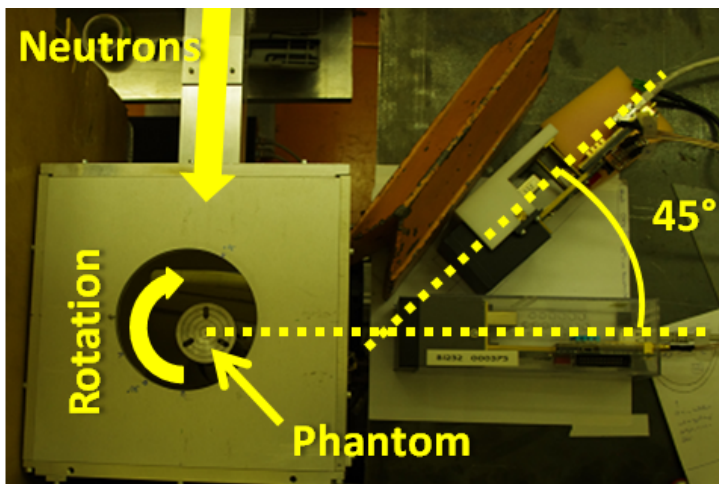
4.4.2 Measurement set-up

The measurement configuration has to be slightly modified due to the different conditions compared to the training reactor. The energy of the neutrons are so low that they would have absorbed in a few mm of polyethylene, the material of our previously used sample holder before they can reach the real object. A new cylindric aluminium sample holder was made with two cylinder hole in it for the samples. In Figure 37(b) the parameters of the phantom are demonstrated.

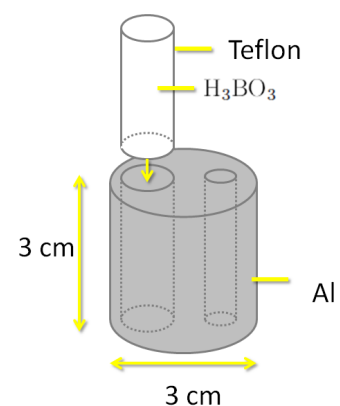
The second necessary modification was the consequence of the difference in the stepping motor. The facility has its own positioning system that we could use. It meant a modification in the C# code that handles the data acquisition from the detectors and the motor movements.

The inclination between the two detectors was θ as before. The distance between the rotation center of the phantom and the front face of the first detector was modified to 15 cm. The set-up is illustrated in Figure 37(a).

As we experienced the only significant signal is coming from boron. Therefore, hereinafter we only used boric acid as prompt- γ source. Since we did not know the exact sensitivity of our detection system for this new set-up, we prepared a set of dissolved boric acid with different concentrations. The solutions were filled in Teflon tubes.



(a) Measurement set-up



(b) Aluminium phantom with boric acid in a Teflon sample holder

Figure 37: Toolkit for the measurement at CNS

4.4.3 Preliminary results

Before collecting data in tomography mode, i.e. alternating the data acquisition and rotation steps, several preliminary calibrations and test were conducted.

An estimation for maximal possible count rate was done. The used parameters are listed in Table 7. The approximation is an upper estimation regarding the efficiencies and the mass of the radiated boron.

m	- Mass of H_3BO_3 in the sample (mg)	:1000
N	- Number of boron atoms in the sample (-)	: $9.68 \cdot 10^{21}$
Φ	- Thermal equivalent neutron flux (<i>number/(cm²s)</i>)	: $2.7 \cdot 10^7$
σ_g	- Thermal equivalent prompt- γ cross section (barn)	:713
ϵ_{geo}	- Geometrical efficiency (-)	:0.0111
$\epsilon_{Compton}$	- Efficiency to detect coincidence events(-)	:0.002

Table 7: Parameters used for count rate estimation

$$cps = \epsilon_{geo} \cdot \epsilon_{Compton} \cdot \Phi \cdot \sigma_g \cdot N \cdot 10^{-24} = 4 \cdot 10^3 \text{ 1/s}$$

So we expected 20 000 coincidence events in a second for using the pure boric acid sample which was not dissolved in water.

In order to tune the required boric acid concentration of the sample, we tested three different samples. In Figure 38 the result of this three test measurements is shown. Each curve is a total released energy spectrum of the coincidence events belonging to a sample with different amounts of boron. First, the Teflon tube was only filled with distilled water. This data gives the basic line for further analysis. In the second case, the mass of boric acid in 1 ml water solution was 50mg. The third Teflon tube contained 1000mg of pure boric acid powder. The count rate calculation above was done according to this amount of boron, so we compares that approximation with this third curve.

The noticeable characteristics are the followings:

- With the increment of the boron mass, the area of the peak at 477 keV is increasing. This observation meets with our expectations. From the data of the samples that contains boron the background can be eliminated with the subtraction of the basic level (the third curve). The increment of the peak area of these reduced graphs is not proportional to the amount of boron. It can be explained with the superficial absorption of the cold neutrons on the surface of the boron cylinder.
- The number of detected coincidence events during one second is in the range of 100. Thus the estimation of the maximal count rate has an order difference compared to the real measurement data. A transmission image can be seen in Figure 39 from

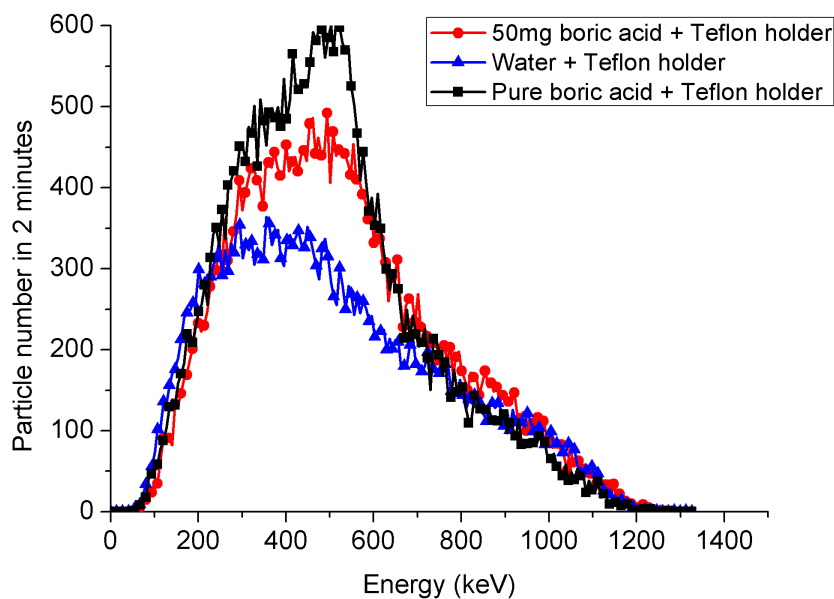


Figure 38: Total released energy spectrum with different amount of boric acid: With the increment of boron mass the peak at 477 keV is increasing.

the phantom with pure boric acid in the Teflon tube. It confirms that the boron absorbs all of the neutrons.

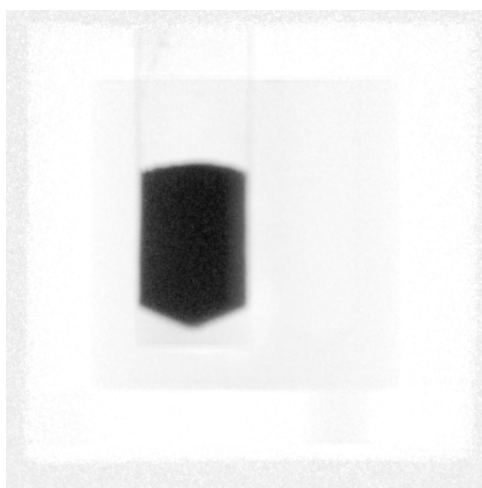


Figure 39: Transmission picture from the phantom with boric acid in Teflon tube.

The check of the detection of the prompt- γ photons were done. The energy calibration was validated again since the peak related to the boron presence appeared around 477 keV.

4.4.4 Image reconstruction

The characteristics of the image reconstruction engine was demonstrated on a case study in section 4.1. Here, the proof of the working method is shown on a series of measurement data coming from neutron activated prompt- γ .

The tomography measurements were done from 18 different angles with a step of 10° . The data was collected for 2 minutes for each projection. So the needed minimal measuring time was 36 minutes. However it is hardly more than half an hour, the preceding processes required more time than it was scheduled. So finally we had only one chance to conduct the whole tomography measurements. Due to an unexpected misbehaving of the synchronization of the data acquisition from the two detectors the number of coincidence events was not satisfying in every projection.

Therefore, finally only 3 projections were selected representing 3 furthest one in angle from each other. The corresponding rotation angles: 90° , 180° and 270° . We decided to shelve the ability of the image reconstruction software to produce three-dimensional reconstruction and demonstrate the results on a more simple two-dimensional reconstruction. The benefit that we gain from this simplification is that the result is at least comparable with the experiences of the case study made by *Cs* – 137 source. The system matrix for the CNS measurements were simulated on a 15×15 voxel grid. Besides the same settings were chosen as for the *Cs* case. With this size the side length of a pixel was 0.27 cm. The running time was 22 hours.

As we learned from the case study with cesium source, the acquired data should be processed before the image reconstruction. Here, 2-pixel-wide edge cut-off and 100 keV total energy window were applied. The difference from the *Cs* case, that now the center of the total energy window is 477 keV instead of the formerly used 662 keV. In order to eliminate corner shining effects, further changes in contrast settings were done. The result can be seen in Figure 40.

Images are seemingly follow the shift due to their spatial positions, while this effect should be by far more apparent. Though the reconstructed source can be clearly seen, due to the low number of successful data acquisitions we cannot conclude any creditable spatial resolution. However even using the same series of data it is expected that with further procedures the results can be improved.

- For example with refined probability response matrix calculations, maybe with using parallel processing. Or the total energy window can be more restricted if a more precise energy calibration is used, since we applied the same linear calibration for all over one detector.
- An advancement can be achieved with pixel-by-pixel energy calibration.

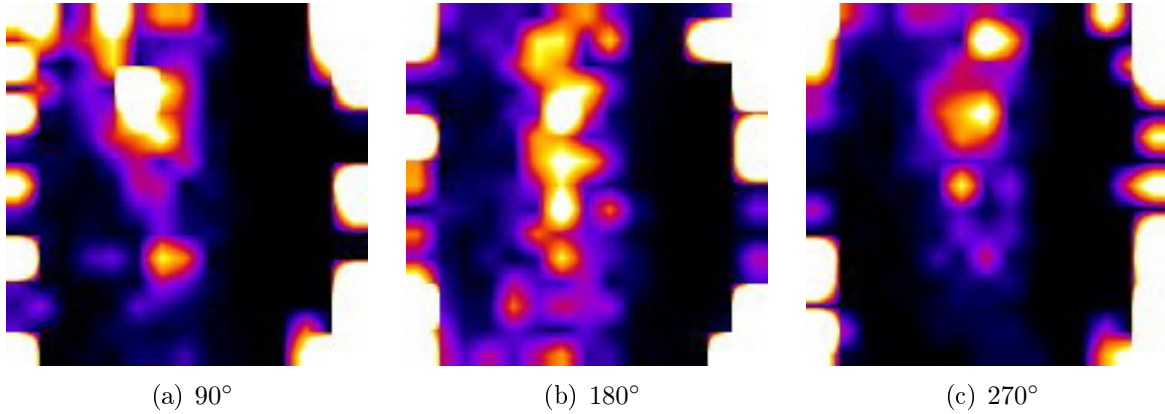


Figure 40: Boron data reconstructions of three projections with different angles with regard to the neutron beam direction

4.4.5 Suggestions for a repeated experiment

- To improve the vertical resolution the absorber should be moved in vertical direction. For example it can be rotated around the principal axis of the scatterer beside rotating the sample around.
- With the help of the simulation software before tomography measurements optimize the number of needed projections and the amount of the angular step in order to get the best reconstructed image quality.
- In order to examine the spatial distribution of more elements in the same time, an additional dimension to the probability matrix has to be added: The total absorbed energy in the two detectors. It could be tested with the same sample holder since the aluminium has quite high neutron capture cross section. It has two significant prompt-gamma energy level in the lower energy ranges: 30 keV and 983 keV. With other voltage settings they can be investigated.

4.5 Limitations of the research

Finally the limitations of the research set-up were collected separated into four main groups.

4.5.1 Detectors

- The own activity of the LYSO scintillation crystal appears as an inconvenient, constant background level. To exceed its disturbing effects high gamma activity has to be used which comes together with higher neutron flux and higher doses.

This fact endangers the possibility of using the discussed configuration for *in vivo* applications. However another detector type can be a solution for this issue.

- Without the accurate pixel-by-pixel energy calibration the maximal available energy resolution can be achieved. Therefore, an experimental series is suggested: Energy spectrum with several calibration sources should be done with the shifting of the sources along the whole detector surface reaching every pixel with the maximum intensity.
- The geometry configuration significantly limited the vertical resolution of the detector system. Hence, the moving or the increased number of the absorber detector should be take into consideration.
- The puffer of the detector sometimes still contains data from a previous measurement, which can modify the newly collected data.

4.5.2 Simulation

- In order to use the simulation software for solving further optimization tasks, the raw data acquired from the simulation and from the measurements should be compared more detailed. For example the pixel-by pixel energy resolution with the broadening of a sodium source photopeak.
- At the moment the simulation software only capable of dealing with a gamma-source. The handling of the neutron transport should be added.

4.5.3 Image reconstruction

- In order to generate larger probability response matrix within shorter time, the software should be supported by parallel processing.

4.5.4 Neutron source

- The repeated experiment at BNC with the ultracold neutrons is worth to be done, since we did not get data with high quality enough at our first attempt. However from the analysis of these handicapped data it is clear that this configuration is promising after a few modification.
- Still a great perspective to try the DT neutron generator as a neutron source since it is almost free of gamma background. The provided neutrons have only one energy with high penetration capability, so the simulation with them is much more easier.

5 Conclusion

The idea of the merging of PGAA and Compton camera was proven useful and key factors influencing the imaging qualities identified.

Concerning the used LYSO detector the following conclusions can be stated:

- In order to make the disturbing effect caused by the background coming from the LYSO own activity less significant the used gamma activity should be quite high. Subsequently the high level of doses can result in overdosing in *in vivo* applications. Therefore the use of a different scintillator material would make a huge difference in the results. However even without LYSO background the decrement of the minimum detectable activity level would need many absorber detectors.
- There were several attempts to optimize the geometry configuration in order to accomplish the best detection efficiency. But it became clear that the main improvement could be moving or adding additional absorber detectors, not the optimization of the detector positions relative to each other.
- Even the better resolution in the horizontal direction should be improved. This can be achieved by the application of a scatterer detector with an energy resolution as high as possible.

Three main and several less significant softwares were made dedicated to the handling of the work with the detector set-up and data analysis. The validation of the Compton camera simulation was done by a comparison to MCNP, the goodness of the image reconstruction program was proved by the fact that the results of real measurement data can be explained. Besides, the following developments are suggested:

- In order to have the opportunity to generate a more detailed system matrix, the speed of the calculation should be improved, perhaps with parallel processing.
- Both the simulation and the image reconstruction software shall be extended for neutron simulations.
- It would be advantageous to develop the software into a state which can tell whether *in vivo* imaging is capable of being conducted for organ constituent isotopes or B, Gd or Cd tracers are needed.

Among the presently available neutron sources the cold neutron source of the Budapest Nuclear Center fulfilled our expectations. However the detector system requires further optimization to this source type.

Acknowledgment

It is with immense gratitude that I acknowledge the support and help of my supervisor, Dávid Légrády. Especially, due to all of his great efforts and constant encouragement to make it feasible to achieve as much as possible during my work.

I would like to thank Gábor Kleizer for his valuable assistance regarding the data acquisition and motor handling softwares and his kindness to build a dedicated table for the detectors.

I consider it an honor to work with István Rovni who gave us a lot of indispensable information on the field of neutron activation analysis and helped us to have the opportunity to perform measurement at Budapest Neutron Center.

I owe my deepest gratitude to Zoltán Kiss and László Szentmiklósi who were so kind giving us the opportunity to use the facility of Cold Neutron Source within weeks and sharing their professional help with us.

This thesis would not have been possible without the support of József Molnár and József Imrek who made it possible for me to use one of the miniPET module of the Institute of Nuclear Research, Debrecen.

I always want to say thank all of my professors, colleagues and students at the Institute of Nuclear Techniques who helped me with their work, discussions and advises.

I would have not finished this project without the support of my family and my boyfriend, Árpád Csata. My friends also deserve my gratitude who were always beside me all my years spent at university. Thank you!

References

- [BOA⁺04] D. Bhattacharya, T.J. O'Neill, A. Akyuz, J. Samimi, and A.D. Zych, *Prototype tigre compton gamma-ray balloon-borne telescope*, NEW ASTRONOMY REVIEWS **48** (2004).
- [BRM06a] P. F. Bloser, J. M. Ryan, and M. L. McConnell, *The mega project for medium energy gamma-ray astronomy*, Chin. J. Astron. Astrophys **6** (2006), 388–392.
- [BRM⁺06b] P. F. Bloser, J. M. Ryan, M. L. McConnell, J. R. Macri, U. Bravar, and G. Kanbach et al, *The mega project for medium energy gamma-ray astronomy*, Chin. J. Astron. Astrophys. **6** (2006), 388–392.
- [CN86] M.E. Casey and R. Nutt, *A multicrystal 2-dimensional bgo detector system for positron emission tomography*, IEEE Transactions on Nuclear Science (1986).
- [DLS⁺98] F. A. Dilmanian, L. J. Lidofsky, I. Stamatelatos, Y. Kamenyk, S. Yasumura, D. Vartskyy, R. N. Pierson Jr, A. Webery, R. I. Moorey, and R. May, *Improvement of the prompt-gamma neutron activation facility at brookhaven national laboratory*, Phys. Med. Biol. **3** (1998), 339–349.
- [DPF⁺09] Carsten Degenhardt, Gordian Prescher, Thomas Frach, Andreas Thon, Rik de Gruyter, Anja Schmitz, and Rob Ballizany, *The digital silicon photomultiplier - a novel sensor for the detection of scintillation light*, IEEE Nuclear Science Symposium Conference Record (2009).
- [FPD⁺09] Thomas Frach, Gordian Prescher, Carsten Degenhardt, Rik de Gruyter, Anja Schmitz, and Rob Ballizany, *The digital silicon photomultiplier - principle of operation and intrinsic detector performance*, IEEE Nuclear Science Symposium Conference Record (2009).
- [FZMP10] Mirela Frandes, Andreas Zoglauer, Voichita Maxim, and Rémy Prost, *A tracking compton-scattering imaging system for hadron therapy monitoring*, TRANSACTIONS ON NUCLEAR SCIENCE **57** (2010), 144–150.
- [GBB⁺09] Alberto Del Guerra, Nicola Belcari, Maria G. Bisogni, Gabriela Llosa, Sara Marcatili, and Sascha Moehrs, *Advances in position-sensitive photodetectors for pet applications*, 604 (2009), 319–322.
- [GMR⁺97] T. Grósz, V.A. Mityukhlyayev, L. Rosta, Serebrov, and A.A. Zaharov, *Liquid hydrogen cold moderator optimisation at the budapest research reactor*, Physica B (1997), 234–236.

- [GX04] R. P. Gardner and L. Xu, *Prompt gamma-ray imaging for small animals*, International Symposium of Biomedical Imaging (2004), 1373–1376.
- [JSB⁺07] C. E. Floyd Jr., A. C. Sharma, J. E. Bender, A. J. Kapadia, J. Q. Xia, B. P. Harrawood, G. D. Tourassi, J. Y. Lo, M. R. Kiser, A. S. Crowell, R. S. Pedroni, R. A. Macri, S. Tajima, and C. R. Howell, *Neutron stimulated emission computed tomography: Background corrections*, Nuclear Instruments and Methods in Physics Research B (2007).
- [KR] J. Kópházi and I. Rovni, *Zone modeling simulation for the nti training reactor*.
- [KST⁺09] A. J. Kapadia, A. C. Sharma, G. D. Tourassi, J. E. Bender, C. R. Howell, A. S. Crowell, M. R. Kiser, B. P. Harrawood, R. S. Pedroni, and C. E. Floyd, *Neutron stimulated emission computed tomography for diagnosis of breast cancer*, TRANSACTIONS ON NUCLEAR SCIENCE (2009).
- [LAB08] OAK RIDGE NATIONAL LABORATORY, *Mcnp4c - monte carlo n-particle transport code system*, 2008.
- [Laj09] Imre Lajtos, *Kisállat vizsgálatokhoz fejlesztett pozitron emissziós tomográf fizikai paramétereinek meghatározása*, Master’s thesis, Debreceni Egyetem Természettudományi és Technológiai Kar, 2009.
- [LCH⁺97] J.W. LeBlanc, N.H. Clinthorne, C-H Hua, E. NygHrd, W.L. Rogers, D.K. Wehe, P. Weilhammer, and S.J. Wilderman, *C-sprint: A prototype compton camera system for low energy gamma ray imaging*, TRANSACTIONS ON NUCLEAR SCIENCE **45** (1997), 943–949.
- [LeB99] James Walter LeBlanc, *A compton camera for low energy gamma ray imaging in nuclear medicine applications*, Ph.D. thesis, University of Michigan, 1999.
- [LK90] Iván Lux and László Koblinger, *Monte carlo particle transport methods: Neutron and photon calculations*, CRC Press, 1990.
- [LL10] W. Lee and T. Lee, *A compact compton camera using scintillators for the investigation of nuclear materials*, Nuclear Instruments and Methods in Physics Research A **624** (2010), 118–124.
- [Maj11] Péter Major, *Nukleáris medicina lecture notes*, 2011.

- [MKW⁺93] J. B. Martin, G. F. Knoll, D. K. Wehe, N. Dogan, V. Jordanov, and N. Petrick, *A ring compton scatter camera for imaging medium energy gamma rays*, *Trans. Nucl. Sci.* **40** (1993), 972–977.
- [Nag06] Károly Nagy, *A compton-kamera elméleti vizsgálata*, Master’s thesis, Budapest University of Technology and Economics, 2006.
- [Orv] <http://oftankonyv.reak.bme.hu>, Medical Physics on-line book.
- [S95] I. E. STAMATELATOS and S. YASUMURA 2, *Prompt-gamma neutron activation facility for measuring body nitrogen in vivo in small animals*, *46 4* (1995), 269–272.
- [SHS73] V. Schönfeldera, A. Hirnera, and K. Schneidera, *A telescope for soft gamma ray astronomy*, *Nuclear Instruments and Methods* **107** (1973), 385–394.
- [SHS79] V. Schönfeldera, A. Hirnera, and K. Schneider, *A telescope for soft gamma ray astronomy*, *Nuclear Instruments and Methods* **107** (1979), 385–394.
- [Sin83] M. Singh, *An electronically collimated gamma camera for single photon emission computed tomography. part i: Theoretical considerations and design criteria*, *Medical Physics* **10** (1983), 421–427.
- [SK10] László Szentmiklósi and Zsolt Kasztovszky, *Prompt gamma aktivációk analitikai gyakorlat*, MTA Institute of Isotopes, 2010.
- [SKP⁺10] Hee Seo, Chan Hyeong Kim, Jin Hyung Park, Jong Kyung Kim, Ju Hahn Lee, Chun Sik Lee, and Jae Sung Lee, *Development of double-scattering-type compton camera with double-sided silicon strip detectors and nai(tl) scintillation detector*, *Nuclear Instruments and Methods in Physics Research A* **615** (2010), 333–339.
- [SLK⁺08] Hee Seo, Se Hyung Lee, Chan Hyeong Kim, So Hyun An, Ju Hahn Lee, and Chun Sik Lee, *Optimal geometrical configuration of a double-scattering compton camera for maximum imaging resolution and sensitivity*, *591* (2008), 80–83.
- [Stu05] Andrej Studen, *Compton camera with position-sensitive silicon detectors*, Master’s thesis, University of Ljubljana Faculty of Mathematics and Physics, 2005.
- [Uch86] H. Uchida, *Design of a mosaic bgo detector system for positron ct*, *IEEE Transactions on Nuclear Science* (1986).

- [vZ06] Éva Zsolnay, *Az nti oktatóreaktor jellemző neutronfluxus adatai*, BME-NTI-345/2006, 2006.
- [YKS⁺11] Mitsutaka Yamaguchi, Naoki Kawachi, Nobuo Suzui, Shu Fujimaki, and Tomihiro Kamiya et al, *Development of head module for multi-head si/cdte compton camera for medical applications*, Nuclear Instruments and Methods in Physics Research Section A **648** (2011), S2–S7.

Appendix

List of abbreviations

BME - Budapest University of Technology and Economics

BNC - Budapest Neutron Center

CNS - Cold Neutron Source

CT - Combined Tomography

DT - Deuterium-Tritium (neutron generator)

EM - Expectation Maximization

FPGA - Field Programmable Gate Array

FWHM - Full Width of Half Maximum

HPGe - High Purity Germanium

LYSO - Lutetium-yttrium-orthosilicate

MC - Monte Carlo

ML - Maximum Likelihood

NAA - Neutron Activation Analysis

NIPS - Neutron [Inducated Photon Spectroscopy](#)

NTI - Institute of Nuclear Techniques

PET - Positron Emission Tomography

PGAA - Prompt Gamma Activation Analysis

PSPMT - Position Sensitive Photomultiplier

PuBe - Plutonium-Beryllium neutron source

SDDS - Double Sided Strip Detector

SiPM - Silicon Photomultiplier

SPD - Silicon Pad Detector

SPECT - Single Positron Emission Tomography

Önállósági nyilatkozat(Declaration of independent work)

Alulírott Hülber Tímea Orvos Fizika MSc szakos hallgató (Neptun kód: T9QEXW) a Transzmissziós, emissziós és gerjesztett gamma tomográfia című diplomamunka szerzője fegyelmi felelősségem tudatában kijelentem, hogy dolgozatom önálló munkám eredménye, saját szellemi termékem, abban a hivatkozások és idézések általános szabályait következetesen alkalmaztam, mások által írt részeket a megfelelő idézés nélkül nem használtam fel.

Budapest, 2012. május 25.